Long-term general relativistic simulation of binary neutron stars collapsing to a black hole

Kenta Kiuchi,[1,*] Yuichiro Sekiguchi,[2,†] Masaru Shibata,[3] and Keisuke Taniguchi[4]

[1]*Department of Physics, Waseda University, 3-4-1 Okubo, Shinjuku-ku, Tokyo 169-8555, Japan*
[2]*Division of Theoretical Astronomy/Center for Computational Astrophysics,*
National Astronomical Observatory of Japan, 2-21-1, Osawa, Mitaka, Tokyo, 181-8588, Japan
[3]*Yukawa Institute for Theoretical Physics, Kyoto University, Kyoto, 606-8502, Japan*
[4]*Department of Physics, University of Wisconsin-Milwaukee, P.O. Box 413, Milwaukee, Wisconsin 53201 USA*

General relativistic simulations for the merger of binary neutron stars are performed as an extension of a previous work [M. Shibata and K. Taniguchi, Phys. Rev. D **73**, 064027 (2006).]. We prepare binary neutron stars with a large initial orbital separation and employ the moving-puncture formulation, which enables one to follow merger and ringdown phases for a long time, even after black hole formation. For modeling inspiraling neutron stars, which should be composed of cold neutron stars, the Akmal-Pandharipande-Ravenhall (APR) equation of state (EOS) is adopted. After the onset of merger, the hybrid-type EOS is used; i.e., the cold and thermal parts are given by the APR and Γ-law EOSs, respectively. Three equal-mass binaries, each with mass $1.4M_\odot$, $1.45M_\odot$, and $1.5M_\odot$, and two unequal-mass binaries with mass, 1.3 vs $1.6M_\odot$ and 1.35 vs $1.65M_\odot$, are prepared. We focus primarily on the black hole formation case, and explore mass and spin of the black hole, mass of disks which surround the black hole, and gravitational waves emitted during the black hole formation. We find that (i) the black hole is promptly formed if total mass of the system initially satisfies $m_0 \gtrsim 2.9M_\odot$; (ii) for the systems of $m_0 = 2.9$–$3.0M_\odot$ and of mass ratio ≈ 0.8, the mass of disks which surround the formed black hole is 0.006–$0.02M_\odot$; (iii) the spin of the formed black hole is 0.78 ± 0.02 when a black hole is formed after the merger in the dynamical time scale. This value depends weakly on the total mass and mass ratio, and is about 0.1 larger than that of a black hole formed from nonspinning binary black holes; (iv) for the black hole formation case, Fourier spectrum shape of gravitational waves emitted in the merger and ringdown phases has a universal qualitative feature irrespective of the total mass and mass ratio, but quantitatively, the spectrum reflects the parameters of the binary neutron stars.

I. INTRODUCTION

Coalescence of binary neutron stars is one of the most promising sources for kilometer-size laser interferometric detectors such as the LIGO [1,2], GEO [3], VIRGO [4,5], and TAMA [6]. Latest statistical estimates indicate that the detection rate of gravitational waves from binary neutron stars will be 1 event per ∼40–300 years for the first-generation interferometric detectors and ∼10–100 events per year for the advanced detectors [7,8]. This suggests that gravitational waves from binary neutron stars will be detected within the next decade.

The merger of the binary neutron stars has also been proposed as a likely candidate for the central engine of short γ-ray bursts (GRBs) [9,10]. The observational facts that short GRBs have a cosmological origin (e.g., Ref. [11]) indicate that the central engine supplies a large amount of energy $\gtrsim 10^{48}$ ergs in a very short time scale ∼0.1–1 s [12]. According to a standard scenario based on the merger hypothesis, a stellar-mass black hole surrounded by a hot and massive disk (or torus) should be formed after the merger. Possible relevant processes to

extract the energy of this black hole-accretion disk system for launching a relativistic jet are neutrino-antineutrino annihilation and magnetically driven mechanisms.

Recent semianalytic calculations (e.g., Ref. [13]) show that an accretion rate of $\dot{M} \gtrsim 0.1M_\odot/\text{s}$ is required for neutrino annihilation models to achieve sufficiently high-energy efficiency. Also, recent numerical studies (e.g., Ref. [14]) suggest that if the disk had a mass $\gtrsim 0.01M_\odot$, it could supply the required energy by neutrino radiation. Recent general relativistic magnetohydrodynamic simulations [15] of this (Kerr) black hole-accretion disk system find that the rotational energy of the black hole can be extracted via magnetohydrodynamics processes as a form of the Poynting flux. In particular, the results are in general agreement with the predictions of Blandford and Znajek [16]. In this case, the black hole is required to be rapidly rotating for efficient energy extraction. This fact motivates one to calculate final mass and spin of the black hole formed after the merger, and to clarify whether such a massive disk can be formed, and to clarify what type of the progenitors are necessary for formation of a system composed of a black hole and a massive disk.

For theoretically studying the late inspiral, merger, and ringdown phases of the binary neutron stars, numerical relativity is a unique approach. Until quite recently, there

*kiuchi@gravity.phys.waseda.ac.jp
†sekig@th.nao.ac.jp

has been no long-term general relativistic simulation that self-consistently clarifies the inspiral and merger phases because of limitation of the computational resources or difficulty in simulating a black hole spacetime, although a number of simulations have been done for qualitative studies [17–24]. The most crucial drawbacks in the previous works are summarized as follows (but, see, Refs. [25,26]); (i) the simulations were not able to be continued for a long time after the formation of a black hole and/or (ii) the simulations were short term for the inspiral phase; the inspiral motion of the binary neutron stars is followed only for ~1–2 orbits. The simulations were usually started with a quasiequilibrium state, which is obtained assuming that approaching velocity between two neutron stars is zero, that is not realistic. As a result of this treatment, nonzero approaching velocity at the onset of the merger is not correctly taken into account, and moreover, effects of nonzero eccentricity could play an disfavored role [27].

In the present work, we perform an improved simulation overcoming these drawbacks: (i) we adopt a moving-puncture approach [30,31], which enables us to evolve black hole spacetimes for an arbitrarily long time; (ii) we prepare binary neutron stars in quasiequilibrium states of a large separation as the initial condition. In the chosen initial data, the binary neutron stars spend ~4 orbits in the inspiral phase before the onset of merger, and hence, approximately correct nonzero approaching velocity and nearly zero eccentricity results. Furthermore, we add a nonzero approaching velocity at $t = 0$. The magnitude of the approaching velocity can be estimated by a post-Newtonian (PN) analysis (see Sec. II for details). Adding the approaching velocity suppresses an artificial orbital eccentricity caused by an incompleteness of the initial conditions [32]. In addition, a nonuniform grid with a sufficiently large computational domain [30,33–35] is employed to perform long-term accurate simulations with a relatively low computational cost.

A long-term simulation of binary neutron stars, in which the inspiral phase is followed for 3–5 orbits, has very recently been performed by Baiotti *et al.* using the polytropic and Γ-law equation of state (EOSs) for modeling the neutron stars [26]. With these simple EOSs, they self-consistently investigated the inspiral, merger, and ringdown processes. However, as is well known, such EOSs are oversimplified for modeling the neutron stars, and hence, the results are only qualitative. In this paper, we perform a long-term simulation not with such simple EOSs but by adopting a nuclear-theory-based EOS. We focus, in particular, on quantitatively clarifying the formation process of a black hole for the case that it is formed promptly (i.e., in the dynamical time scale ~1–2 ms) after the onset of merger. More specifically, the primary purpose of this paper is (1) to determine the condition for prompt black hole formation, (2) to determine the final mass and spin of

the black hole formed after the merger, (3) to clarify quantitative features of gravitational waves emitted in the merger and ringdown phases, and (4) to estimate the mass of disks surrounding the formed black hole.

Here, some words of explanation are necessary about nuclear-theory-based EOS (often referred to as realistic EOS). There are two types of nuclear-theory-based EOSs for modeling the neutron stars. One is zero-temperature nuclear EOS such as the Akmal-Pandharipande-Ravenhall (APR) EOS [36]. This type of EOS could be suitable for modeling not so young neutron stars, such as neutron stars in binary neutron stars just before the merger, for which the thermal energy per nucleon is much smaller than the Fermi energy. The other is a finite-temperature EOS such as the Shen's EOS [37]. This type of EOSs should be employed for studying high-energy phenomena such as supernova core collapse and the merger phase of binary neutron stars.

One problem faced when choosing EOSs is that no one knows the truly realistic EOS for high-density nuclear matter. This implies that for studying the inspiral and merger phases of binary neutron stars by numerical simulation, it is necessary to systematically perform many simulations adopting a variety of nuclear-theory-based EOSs. Indeed, one of the important roles in gravitational-wave detection is to constrain nuclear EOS from detected gravitational waves [2]. For this purpose, numerical simulation for a variety of EOSs has to be performed for deriving all the possible gravitational waveforms. There are many cold EOSs that have been proposed [38], and a systematic theoretical survey of the gravitational waveforms for clarifying their dependence on the EOSs is possible. By contrast, there are only a few finite-temperature EOSs [37,39]. This implies that a systematic study is not possible when adopting the finite-temperature EOSs.

In the series of our papers [17,20,21], we have found that shock heating during the merger phase increases the thermal energy of the neutron stars. This indicates that adopting finite-temperature EOSs is desirable for a sophisticated study of the merger process. However, the shock heating is not very strong during the merger and the thermal energy per nucleon after the shock heating is only ~10% of the Fermi energy of the nuclear matter in the central region of the merged object (see Sec. IV). Thus, the thermal energy is not essential at least for short-term evolution of the main body of the merged object. In particular, the thermal energy plays a minor role in determining the criterion for prompt black hole formation at the merger and its process. Because of this reason, in the previous two papers [17,22], we have adopted a hybrid EOS in which the pressure and thermal energy are divided into cold and hot parts. The cold part is determined by the zero-temperature nuclear-theory-based EOSs, and the hot part is simply modeled by a Γ-law EOS. In this method, the main part (cold part) of the EOS is appropriately modeled, although a minor part

(finite-temperature part) is modeled in an approximate manner. The merit of this EOS is that a variety of the cold EOSs can be systematically employed for the simulation. The hybrid EOS may not be appropriate for studying the long-term evolution of a hypermassive neutron star which is formed when the total mass of the system is not large enough for prompt black hole formation. The reason for this is that in the hypermassive neutron star, long-term shock heating and cooling via neutrino emission are likely to play a role. However, for studying prompt black hole formation, which is the main subject of this paper, the hybrid EOS seems to be acceptable because the roles of the shock heating and neutrino cooling do not seem to be essential. Thus, following previous papers [17,22], numerical simulations are performed, employing the hybrid EOS. Specifically, we adopt the APR EOS for the cold part following Ref. [17].

This paper is organized as follows. In Sec. II, we describe the formalism for numerical solution of the Einstein and of relativistic-hydrodynamics equations, the EOS adopted in this paper, and the method for extraction of gravitational waves. The initial condition for binary neutron stars and grid structure for the simulation are summarized in Sec. III. In Sec. IV, numerical results are presented, focusing, in particular, on the case that a black hole is formed in the dynamical time scale after the onset of merger. Section V is devoted to a summary. Throughout this paper, unless otherwise stated, we adopt the geometrical units in which $G = c = 1$ where G and c are the gravitational constant and the speed of light. Greek and Latin indices denote the spacetime and space components, respectively.

II. FORMULATION

A. Numerical methods

Our formulation for the fully general relativistic simulation is the same as in Refs. [17,21,34], to which the reader may refer for details of the basic equations.

For solving the Einstein evolution equations, we use the original version of the Baumgarte-Shapiro-Shibata-Nakamura formalism [40]: We evolve the conformal factor, $\phi = (\ln\gamma)/12$, the trace part of the extrinsic curvature, K, the conformal three-metric, $\tilde{\gamma}_{ij} \equiv \gamma^{-1/3}\gamma_{ij}$, the trace-free extrinsic curvature, $\tilde{A}_{ij} \equiv \gamma^{-1/3}(K_{ij} - K\gamma_{ij}/3)$, and a three-auxiliary variable, $F_i \equiv \delta^{jk}\partial_j\tilde{\gamma}_{ik}$. Here γ_{ij} is the three metric, K_{ij} the extrinsic curvature, $\gamma \equiv \det(\gamma_{ij})$, and $K \equiv K_{ij}\gamma^{ij}$. As in Ref. [34], we evolve the conformal factor ϕ, not the inverse of ψ, because the cell-centered grid is adopted in our code, and hence, the coordinate singularity at the puncture is avoided in moving-puncture frameworks [30,31].

For the conditions of the lapse, α, and the shift vector, β^i, we adopt a dynamical gauge condition in the following forms:

$$(\partial_t - \beta^i\partial_i)\ln\alpha = -2K, \quad (2.1)$$

$$\partial_t\beta^i = 0.75\tilde{\gamma}^{ij}(F_j + \Delta t\partial_t F_j), \quad (2.2)$$

where Δt denotes the time step in the numerical simulations, and the second term on the right-hand side of Eq. (2.2) is introduced for stabilizing the numerical computations. The gauge condition (2.2), which was originally proposed in Ref. [41], is slightly different from that usually used in the moving-puncture framework (see, e.g., [26]). We note that Ref. [25] shows that this gauge is as suitable as the popular one for simulating black hole spacetimes.

The numerical scheme for solving the Einstein equations is essentially the same as that in Ref. [25]. We use the fourth-order finite difference scheme in the spatial direction and a fourth-order Runge-Kutta scheme in the time integration, where the advection terms such as $\beta^i\partial_i\phi$ are evaluated by a fourth-order upwind scheme, as proposed in Ref. [31]. In a previous unigrid simulation, we use a third-order scheme for the time integration [34]. We have found that the fourth-order scheme can give more accurate results, and hence, updated the scheme for this work.

The location and properties of the black hole, such as the area and the circumferential radii, are determined by analyzing an apparent horizon. Our method for finding the apparent horizon is described in Refs. [42,43]. From the area, and polar and equatorial circumferential proper lengths, we infer the mass and spin of the black hole.

The numerical code for the hydrodynamics is the same as that in Refs. [33,34]: As the variables to be evolved, we adopt $\rho_* \equiv \rho\alpha u^t e^{6\phi}$, $\hat{u}_i \equiv hu_i$, and $e_* \equiv h\alpha u^t - P/(\rho\alpha u^t)$, where ρ is the rest-mass density, u_i is the three component of the four velocity, u^t is the time component of the four velocity, P is the pressure, h is the specific enthalpy defined by $h \equiv 1 + \varepsilon + P/\rho$, and ε is the specific internal energy. To handle advection terms in the hydrodynamic equations, a high-resolution central scheme [44] is adopted with a third-order piecewise parabolic interpolation and with a steep min-mod limiter. In the present work, the limiter parameter, b, is set to be 2.5 (see Ref. [45] for details about our interpolation scheme and the parameter b).

B. Equations of state

Following Refs. [17,21], we adopt a hybrid EOS for modeling the EOS of neutron stars. In this EOS, the pressure and the specific internal energy are written in the form

$$P = P_{\text{cold}} + P_{\text{th}}, \quad (2.3)$$

$$\varepsilon = \varepsilon_{\text{cold}} + \varepsilon_{\text{th}}, \quad (2.4)$$

where P_{cold} and $\varepsilon_{\text{cold}}$ are the cold (zero-temperature) parts, and are written as functions of rest-mass density ρ. In general, any nuclear-theory-based EOS for zero-

temperature nuclear matter can be employed for assigning P_{cold} and $\varepsilon_{\mathrm{cold}}$. In this paper, we adopt the APR EOS [36], for which P and ε are tabulated as functions of the baryon rest-mass density for a wide density range. We use a fitting formula for the data in the range, 10^{10} g/cm$^3 \leq \rho \lesssim 10^{16}$ g/cm^3. The method of the fitting was first developed in Ref. [46] and slightly modified in Refs. [17,22]. We adopt the fitting parameters listed in Table I of Ref. [17].

P_{th} and $\varepsilon_{\mathrm{th}}$ in Eqs. (2.3) and (2.4) denote thermal (finite-temperature) parts which are zero in the absence of shocks, but become nonzero if shocks are formed. Specifically, they have finite values after the merger sets in. During the simulation, ρ and ε are determined from the evolved variables ρ_*, e_*, and the normalization relation of the four velocity. Then, $\varepsilon_{\mathrm{th}}$ is determined by $\varepsilon - \varepsilon_{\mathrm{cold}}(\rho)$, and subsequently, the thermal part of the pressure P_{th} is related to the specific thermal energy $\varepsilon_{\mathrm{th}} \equiv \varepsilon - \varepsilon_{\mathrm{cold}}$ as

$$P_{\mathrm{th}} = (\Gamma_{\mathrm{th}} - 1)\rho\varepsilon_{\mathrm{th}}, \qquad (2.5)$$

where Γ_{th} is an adiabatic constant for which we set $\Gamma_{\mathrm{th}} = 2$ taking into account the fact that the EOSs for high-density nuclear matter are stiff.

C. Extracting gravitational waves

To extract gravitational waves from numerical data, we compute the outgoing component of the Newman-Penrose quantity Ψ_4 (e.g., Refs. [25,31,47] for detail). From Ψ_4, loss rates of energy and angular momentum carried by gravitational waves are computed by

$$\frac{dE}{dt} = \lim_{r\to\infty}\left[\frac{r^2}{16\pi}\oint_S d(\cos\theta)d\varphi\left|\int^t \Psi_4 dt'\right|^2\right], \quad (2.6)$$

$$\frac{dJ}{dt} = \lim_{r\to\infty}\mathrm{Re}\left[\frac{r^2}{16\pi}\oint_S d(\cos\theta)d\varphi\left(\int^t \partial_\varphi \Psi_4 dt'\right)\right.$$
$$\left. \times\left(\int^t\int^{t'} \bar{\Psi}_4 dt' dt''\right)\right], \qquad (2.7)$$

where $\oint d(\cos\theta)d\varphi$ denotes an integral on two surfaces of a constant coordinate radius and $\bar{\Psi}_4$ is the complex conjugate of Ψ_4. In numerical simulation, the surface integral is performed for several radii near the outer boundaries, and we check that the resulting gravitational waveforms depend only weakly on the extracted radii. The outer boundaries along each axis are located at $r = L \sim \lambda_0$ where λ_0 is a wave length of gravitational waves emitted by inspiraling binary neutron stars at $t = 0$ and gravitational waves are extracted for $r \approx 0.7 - 0.95L$ (cf. Table II; maximum extraction radii are denoted by r_{ex} in this table).

The amplitude and phase of gravitational waves extracted at several radii should be extrapolated to obtain those at infinity for deriving precise waveforms, as often done in the simulation for binary black holes [32,48–51]. However, numerical waveforms computed in hydrody-

namic simulation are not as precise as those in the simulations for vacuum spacetime, because the order of the accuracy is reduced at shocks, discontinuities, and places where the gradient of hydrodynamic quantities is large in the standard numerical hydrodynamics. This implies that numerical error is primarily determined by such sources, and hence, the finiteness of the extraction radius does not become the main source of the numerical error. To illustrate this fact, we generate Fig. 1 which shows the time evolution of gravitational-wave amplitude for a typical model in this paper. The amplitude $A(t)$ is defined from Ψ_4 as

$$r\Psi_4 = A(t)e^{i\phi(t)}, \qquad (2.8)$$

where r is the extraction radius and ϕ the phase. This plot shows that the amplitude depends very weakly on the extraction radius; relative difference among three results is much smaller than 1%, typical error size induced by the poor resolution of hydrodynamics mentioned above. Thus, we do not use extrapolation of amplitude and wave phase in this work.

For calculating the two polarization modes $h_{+,\times}$ from Ψ_4, we perform the time integration of Ψ_4 twice with the appropriate choice of integration constants and subtraction of unphysical drift, perhaps associated primarily with the drift of the mass center of the system, that often occurs in hydrodynamic simulation due to accumulation of numerical error. Specifically, whenever the time integration is performed, we subtract a function of the form $a_2 t^2 + a_1 t + a_0$ where a_0–a_2 denote constants which are determined by the least-square fitting to the original numerical data.

From a time sequence of dE/dt and dJ/dt, we compute total radiated energy and angular momentum by time integration as

$$\Delta E = \int dt \frac{dE}{dt}, \qquad (2.9)$$

$$\Delta J = \int dt \frac{dJ}{dt}. \qquad (2.10)$$

D. Comparison with PN approximation

Gravitational waveforms in the inspiral phase computed in numerical simulation should be compared with those by the PN approximation, because it provides an accurate waveform if the orbital velocity v is not extremely relativistic (i.e., $v \lesssim 0.3c$). Assuming that binary components are point masses and their quasicircular orbits evolve adiabatically, orbital evolution of the binary stars can be analytically determined with 3PN accuracy and gravitational waveforms are derived with the 3.5PN accuracy [52]. Recently, several phenomenological prescriptions for improving the PN results, which is applicable even to highly relativistic orbits of $v \sim 0.3c$, have been proposed. Among them, high-accuracy simulations for equal-mass and nonspinning binary black holes [32] have proven that the so-
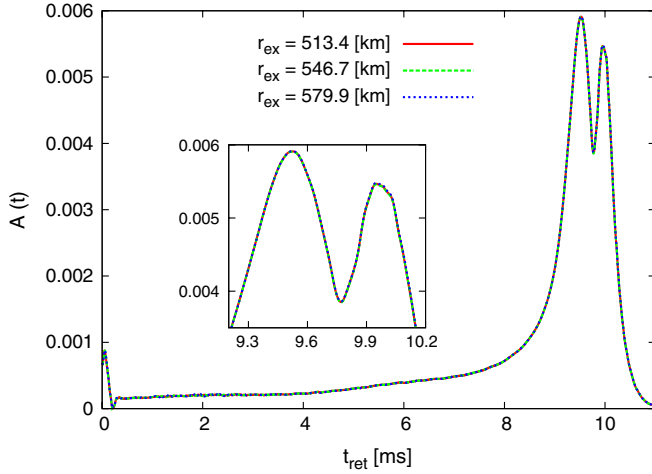
FIG. 1 (color online). The gravitational-wave amplitude as a function of retarded time for run APR145145H. The solid, dashed, and dotted curves denote the amplitudes extracted at 513.4, 546.7, and 579.9 km, respectively.

called Taylor T4 formula provides the orbital evolution and gravitational waveforms with a high accuracy at least up to about one orbit before the onset of the merger. The Taylor T4 formula appears to be a good approximation also for unequal-mass and nonspinning binaries [53] (but see Ref. [54] for a depression of the accuracy for the Taylor T4 in spinning cases). Because we focus only on nonspinning binaries, it is safe to assume that the Taylor T4 formula would be a good approximate formula, and thus, we explore a match between the numerical and Taylor T4's waveforms for the inspiral phase.

One issue in comparison in the present context is that the effect of tidal deformation of neutron stars, which is not taken into account in the Taylor T4 formula, plays an important role for close orbits. This implies that the numerical waveforms should not agree with the waveforms by the Taylor T4 formula for such orbits. Thus, we compare two waveforms for $m_0\Omega \lesssim 0.04$ (see Sec. III A for the definition of m_0).

More specifically, in comparison, two waveforms have to appropriately align as was done in Refs. [32,48,55]. Our procedure in this work is as follows: First we calculate the orbital angular velocity by $\Omega \equiv d\Phi/dt$. Then, we determine the reference time at which two waveforms give the same value of Ω. Recent studies in the context of the binary black holes have shown that the reference value of Ω should be $\lesssim 0.1/m_0$ because beyond this value the PN approximation breaks down [32,47,48,56]. For the binary neutron stars, the value of $0.1/m_0$ is even too large because the compactness of neutron stars is much smaller than that of black holes and hence the merger already started at such

a high value. Also, the effect of tidal deformation of neutron stars plays an important role for $m_0\Omega \gtrsim 0.04$. Because of this reason, the reference value of Ω is chosen to be $m_0\Omega \approx 0.04$ for all the runs in this paper.

III. INITIAL MODEL AND SIMULATION SETTING

A. Initial model

Except for the orbit just before the merger, binary neutron stars are in a quasicircular orbit because the time scale of gravitational radiation reaction at Newtonian order $\sim (5/64)\Omega^{-1}(M\Omega)^{5/3}$ (see, e.g., [57]) is several times longer than the orbital period. Hence, following our previous works [17,21,25,33,34,43], we adopt binary neutron stars in quasiequilibrium states as initial conditions. The quasiequilibrium states are computed in the so-called conformal-flatness formalism for the Einstein equations [58]. The irrotational velocity field is assumed because it is considered to be a realistic velocity field for coalescing binary neutron stars in nature [59,60]. We employ numerical solutions computed by a code in the LORENE library [61–64]. Table I lists the several key quantities for the models adopted in this paper. We select three equal-mass (APR1414, APR145145, and APR1515) and two unequal-mass models (APR1316 and APR135165). Note that the numbers in the model name denote the Arnowitt-Deser-Misner (ADM) mass of the two neutron stars in isolation (e.g., for APR1316, mass of two neutron stars in isolation is $m_1 = 1.3M_\odot$ and $m_2 = 1.6M_\odot$). In the following, we use m_0, M_0, and M_* as the sum of masses of two neutron stars in isolation ($m_0 = m_1 + m_2$), initial total ADM mass, and total rest mass of the system, respectively.

B. Grid setting

In the simulation, the cell-centered Cartesian, (x, y, z), grid is adopted. In these coordinates, we can avoid the situation that the location of the puncture (which always stays on the $z = 0$ plane) coincides with one of the grid points. Equatorial plane symmetry is also assumed. The computational domain of $-L \leq x \leq L$, $-L \leq y \leq L$, and $0 \leq z \leq L$ is covered by the grid size $(2N, 2N, N)$ for (x, y, z), where L and N are constants. Following Refs. [33,34], we adopt a nonuniform grid as follows; an inner domain is covered with a uniform grid of spacing Δx and with the grid size, $(2N_0, 2N_0, N_0)$. Outside this inner domain, the grid spacing is increased according to the relation, $\xi \tanh[(i - N_0)/\Delta i]\Delta x$, where i denotes the ith grid point in each positive direction, and N_0, Δi, and ξ are constants. Then, the location of the ith grid, $x^k(i)$, in each direction is

$$x^k(i) = \begin{cases} (i + 1/2)\Delta x & 0 \leq i \leq N_0 \\ (i + 1/2)\Delta x + \xi\Delta i\Delta x \log[\cosh\{(i - N_0)/\Delta i\}] & i > N_0 \end{cases} \tag{3.1}$$

TABLE I. List of several key quantities for the initial data of binary neutron stars in quasiequilibrium state. The ADM mass of each star when they are in isolation (m_1 and m_2), the maximum baryon rest-mass density for each star, the baryon mass ratio $Q_M \equiv M_{*2}/M_{*1}$, the total baryon rest mass M_*, the total ADM mass M_0, nondimensional spin parameter J_0/M_0^2, orbital period P_0, and the orbital angular velocity in units of M_0^{-1}, $M_0\Omega_0$, where Ω_0 denotes initial orbital angular velocity.

Model	$m_1, m_2(M_\odot)$	$\rho(10^{15} \text{ g/cm}^3)$	Q_M	$M_*(M_\odot)$	$M_0(M_\odot)$	J_0/M_0^2	P_0(ms)	$M_0\Omega_0$
APR1414	1.40, 1.40	0.887, 0.887	1.00	3.106	2.771	0.983	3.185	0.0269
APR145145	1.45, 1.45	0.935, 0.935	1.00	3.232	2.870	0.983	3.299	0.0269
APR1515	1.50, 1.50	0.961, 0.961	1.00	3.359	2.969	0.983	3.412	0.0269
APR1316	1.30, 1.60	0.864, 1.015	0.7943	3.238	2.870	0.976	3.299	0.0269
APR135165	1.35, 1.65	0.887, 1.045	0.7992	3.365	2.970	0.978	3.412	0.0269

and $x^k(-i-1) = -x^k(i)$, where $i = 0, 1, \cdots N$ for $x^k = x$, y, and z. The chosen parameters of the grid structure for each simulation are listed in Table II.

For investigating convergence of numerical results, we perform simulations with three grid resolutions for all the models; labels "L", "M", and "H" denote the low, medium, and high-grid resolutions. We note that for all the runs, the grid resolution around the neutron stars is much better than that in the previous work [17], in which the major diameter of the neutron stars is covered only by 45 grid points. Since it is covered by $\approx$ 60–80 grid points, we expect that numerical results in this paper are much more accurate than those in the previous work. In physical units, the grid spacing around the neutron stars are about 200 m for the highest grid resolution. On the other hand, the grid spacing in a wave zone, where gravitational waves are extracted, is $\approx$ 4 km. The radius of the apparent horizon that the black hole finally formed is covered by about ten grid points.

For high-resolution run (run "H"), about 200 GBytes computational memory is necessary and 240 CPU hours was spent using 512 processors on the Cray XT4 system at the Center for Computational Astrophysics in the National Astronomical Observatory of Japan. For run "L", the computational time is $\sim$100 CPU hours using the same processors.

C. Approaching velocity

In computing quasiequilibrium states in the conformal-flatness formalism, approaching velocity, which should be present in reality due to gravitational radiation reaction, is not taken into account. Lack of the approaching velocity induces a nonzero orbital eccentricity and resulting modulation in gravitational waveforms (e.g., Ref. [32]). If a simulation is started from an initial condition in which the initial orbital separation is sufficiently large, the value of the approaching velocity is negligible, and hence, its lack is not a serious problem; in such a case, the approach-

TABLE II. Parameters for the grid structure employed in the numerical simulation. The grid number for covering one positive direction (N), that for the inner uniform grid zone (N_0), the parameters for nonuniform-grid domain ($\Delta i, \xi$), the approximate grid number for covering the major diameter of massive neutron star (L_{NS}), the ratio of the outer grid spacing to the wavelength of fundamental quasinormal mode of the formed black hole (λ_{QNM}), the ratio of the location of outer boundaries along each axis to the initial gravitational-wave length ($\lambda_0 = \pi/\Omega_0$) and maximum radius of gravitational-wave extraction, r_{ex}, in units of kilometer (and in units of L). The last column shows the final outcome; BH and NS denote a black hole and neutron star, respectively.

Model	N	N_0	Δi	ξ	$L_{\text{NS}}/\Delta x$	L/λ_0	$\lambda_{\text{QNM}}/\Delta x$	$r_{\text{ex}}(r_{\text{ex}}/L)$	Outcome
APR1414L	224	114	30	15	60	0.97	$\cdots$	$4.15e+2$ (0.90)	NS
APR1414M	234	120	30	17.5	70	0.98	$\cdots$	$4.35e+2$ (0.94)	NS
APR1414H	253	139	30	20	80	0.97	$\cdots$	$4.28e+2$ (0.93)	NS
APR145145L	224	110	30	20	60	1.24	7.0	$4.41e+2$ (0.72)	BH
APR145145M	252	123	30	20.5	70	1.24	8.3	$5.67e+2$ (0.92)	BH
APR145145H	282	141	30	21	80	1.24	9.2	$5.80e+2$ (0.95)	BH
APR1515L	224	114	30	19.5	60	1.10	7.3	$5.06e+2$ (0.90)	BH
APR1515M	250	128	30	20	70	1.09	8.3	$5.24e+2$ (0.94)	BH
APR1515H	280	145	30	21	80	1.10	9.6	$5.42e+2$ (0.94)	BH
APR1316L	239	130	30	19	60	1.11	7.7	$5.05e+2$ (0.92)	BH
APR1316M	278	160	30	20	70	1.10	8.6	$4.93e+2$ (0.91)	BH
APR1316H	300	170	30	21	80	1.11	9.5	$5.13e+2$ (0.94)	BH
APR135165L	240	130	30	20	60	1.11	7.8	$5.15e+2$ (0.90)	BH
APR135165M	278	155	30	20.5	70	1.11	8.9	$5.14e+2$ (0.90)	BH
APR135165H	310	175	30	21	80	1.10	9.9	$5.19e+2$ (0.92)	BH

ing velocity settles to a correct one and eccentricity approaches zero in a few orbits, because of gravitational radiation reaction [65]. However, in the present choice of the initial condition, the initial orbital separation is not sufficiently large. Thus, we initially add an approaching velocity to improve the quality of the initial condition. For calculating an approximate value of the approaching velocity, we assume that the two neutron stars may be approximated by point particles and the so-called Taylor T4 formula [32,47] is used for predicting their orbital motion. In the following, we describe our method (see relevant works [47,66,67] in simulations of binary black holes): Assuming that the density maxima of the neutron stars are located along the x axis at $t = 0$, the approaching velocity v^x may be calculated by

$$v^x = \frac{dr_{12}}{dt} = -\frac{Gm_0}{\gamma_{12}^2 c^2} \frac{d\gamma_{12}}{dt}, \qquad (3.2)$$

where $\gamma_{12} \equiv Gm_0/r_{12}c^2$ and r_{12} is a coordinate orbital separation in the harmonic gauge. m_0 is the total mass defined by the sum of masses of two neutron stars at a state when they are in isolation. Here, we recover G and c to explicitly clarify that γ_{12} is dimensionless. γ_{12} is written by a gauge-invariant quantity, $x \equiv (Gm_0\Omega/c^3)^{2/3}$, at 3PN order as

$$\gamma_{12} = x\left[1 + \left(1 - \frac{\nu}{3}\right)x + \left(1 - \frac{65}{12}\nu\right)x^2 + \left(1 + \left[-\frac{2203}{2520}\right.\right.\right.$$
$$\left.\left.\left. - \frac{41}{192}\pi^2 - \frac{22}{3}\ln\left(\frac{r_{12}}{r_0'}\right)\right]\nu + \frac{229}{36}\nu^2 + \frac{1}{81}\nu^3\right)x^3\right], \qquad (3.3)$$

where Ω denotes the orbital frequency, $\nu = m_1 m_2/m_0^2$ is the ratio of the reduced mass to the total mass with $m_1(m_2)$ being the mass of the star 1 (2) in isolation, and r_0' is "logarithmic barycenter" [52]. In the Taylor T4 formula [32], the evolution equation of x is derived in an adiabatic approximation as

$$\frac{dx}{dt} = \frac{16c^3}{5Gm_0}x^5\left\{1 - \frac{487}{168}x + 4\pi x^{3/2} + \frac{274\,229}{72\,576}x^2\right.$$
$$- \frac{254}{21}\pi x^{5/2} + \left[\frac{178\,384\,023\,737}{3\,353\,011\,200} + \frac{1475}{192}\pi^2\right.$$
$$\left. - \frac{1712}{105}\gamma_E - \frac{856}{105}\ln(16x)\right]x^3 + \left. \frac{3310}{189}\pi x^{7/2}\right\}, \qquad (3.4)$$

where γ_E is Euler's constant. From Eqs. (3.2), (3.3), and (3.4), the approaching velocity is derived.

We note that this approaching velocity is not gauge invariant and has a strict meaning only in the harmonic gauge condition. Because the initial condition is not obtained in this gauge condition, it would be necessary to carry out a coordinate transformation to obtain the approaching velocity in our chosen gauge condition.

However, the initial condition is obtained in the conformal-flatness formalism, and thus, the gauge condition is not clear, because the metric components are oversimplified in this formalism. Thus, in this work, we use the approaching velocity defined in Eq. (3.2) with no modification. After calculating v^x, the four velocity is modified from its quasiequilibrium value $u_i^{(eq)}$ by adding a correction $u_x^{corr} = we^{4\phi}v^x/\alpha$ with $w \equiv \alpha u^t = (1 + \gamma^{ij}u_i^{(eq)}u_j^{(eq)})^{1/2}$ where we drop a correction in α and β^i due to the change of u_i, because they only give higher-order corrections. Then, we uniformly add the specific momentum hu_x^{corr} to each neutron star and reimpose the Hamiltonian and momentum constraints. Note that it is nontrivial to relate velocity to momentum in general relativity (but see Ref. [68] for discussion about this issue).

Figure 2 plots the evolution of a coordinate orbital separation $I^{1/2}$ with/without approaching velocity for model APR1515. Here, I is defined by

$$I = \frac{I_{xx} + I_{yy}}{M_*}, \qquad (3.5)$$

where $I_{ij} \equiv \int \rho \alpha u^t x^i x^j \sqrt{\gamma} d^3 x$ with u^t being a time component of the four velocity. In the absence of the approaching velocity, I does not decrease monotonically but oscillates with time (the dotted curve in Fig. 2). In the presence of the approaching velocity, this oscillation is suppressed (the solid curve in Fig. 2). This figure illustrates the advantage of our treatment. It should be noted that the orbital eccentricity is not completely suppressed even in this method. As discussed in Sec. IV C 1, indeed, gravitational waveforms in an early phase slightly disagree with that calculated in the Taylor T4 framework (e.g., angular velocity computed by gravitational waves does not increase monotonically but has a modulation; see Sec. IV C 1). However, the radiation reaction circularizes the binary orbit and gravitational waves in the late inspiral
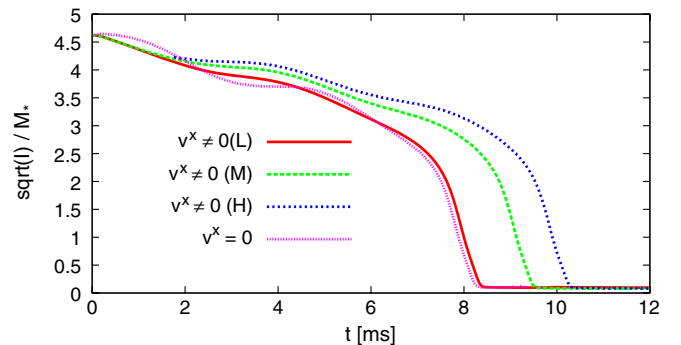

FIG. 2 (color online). The evolution of a coordinate separation defined by Eq. (3.5) for model APR1515. The solid, dashed, and short-dashed curves show the results for runs APR1515L, M, and H with approaching velocity, respectively. The dotted curve does for run APR1515L without approaching velocity.
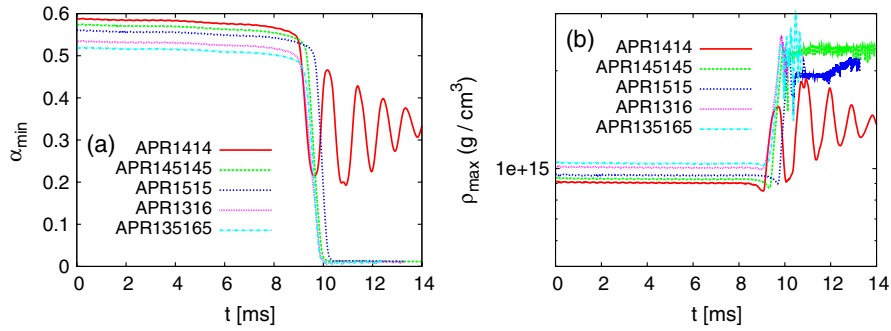
FIG. 3 (color online).   The evolution of the minimum value of the lapse function, $\alpha_{\min}$, and the maximum rest-mass density $\rho_{\max}$ for runs APR1414H, APR145145H, APR1515H, APR1316H, and APR135165H.

phase agree approximately with the prediction by the Taylor T4 formula in a better manner [cf. Fig. 13(b)].

IV. RESULT

A. General feature for merger process

We have already performed simulations for binary neutron stars employing nuclear-theory-based EOSs [17,22]. Although the qualitative feature for the merger process

found in the present work is the same as in the previous works, we here summarize generic feature of the merger again.

Figure 3 plots the evolution of the minimum value of the lapse function, $\alpha_{\min}$, and maximum baryon rest-mass density, $\rho_{\max}$, for all the models studied in this paper. For models APR145145, APR1515, APR1316, and APR135165 for which a black hole is formed in the dynamical time scale ($\sim \rho^{-1/2}$), $\alpha_{\min}$ ($\rho_{\max}$) decreases (in-
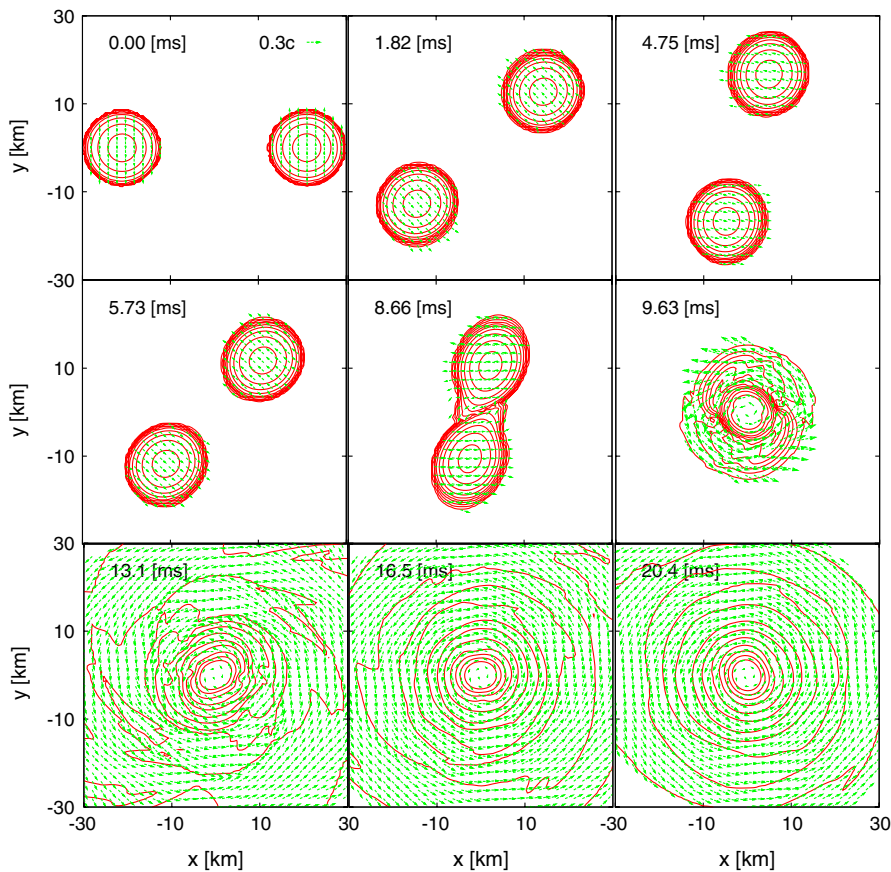
FIG. 4 (color online).   Snapshots of the density contour curves for ρ and velocity field (v^x, v^y) on the equatorial plane for run APR1414H. The solid contour curves are drawn for $\rho = i \times 2 \times 10^{14}$ g/cm^3($i = 1, 2, \cdots$) and for $1 \times 10^{14-0.5i}$ g/cm^3($i = 1 \sim 6$). The time shown in the upper-left side denotes the elapsed time from the beginning of the simulation.
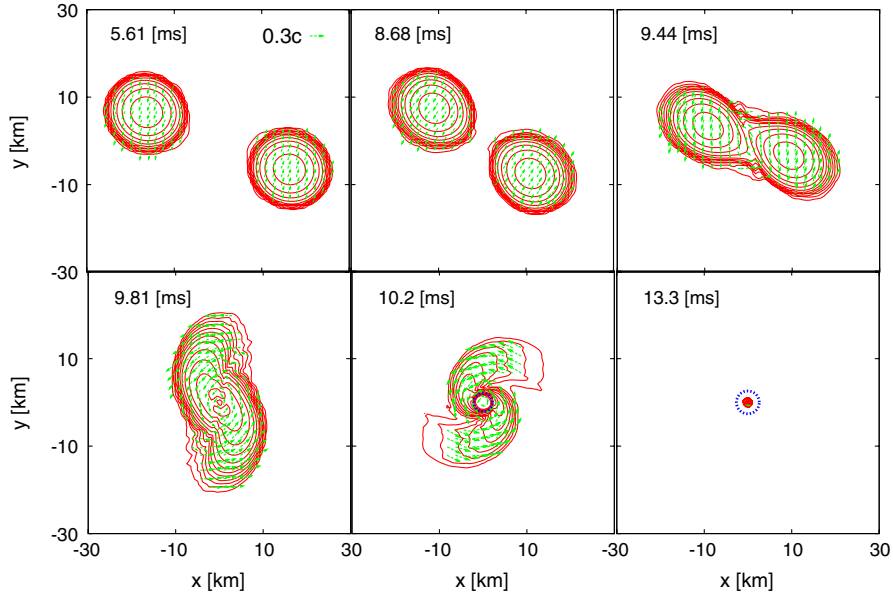
FIG. 5 (color online). The same as Fig. 4 but for run APR1515H. The short-dashed circles around the origin in the last two panels denote the location of the apparent horizon.

creases) monotonically after the onset of the merger. In the high-resolution runs for these models, two neutron stars come into the first contact at $t \sim 9$ ms. This merger time is slightly underestimated because of the effect of finite grid resolution, but the numerical results in the chosen grid resolution is in a convergent regime as discussed in Sec. IV C 1. For all the cases, an apparent horizon is formed when α_{min} reaches ~ 0.03. For model APR1414, α_{min} (ρ_{max}) steeply decreases (increases) after the onset of the merger, but then, they start oscillating and eventually settle down to relaxed values. This indicates that the out-

come is a hypermassive neutron star, for which the baryon rest mass is $\sim 30\%$ larger than the maximum allowed mass of the spherical neutron stars [69].

Figures 4–6 display the evolution of density contour curves for the rest mass in the equatorial plane of the inspiral, merger, and ringdown phases for runs APR1414H, APR1515H, and APR1316H, respectively. For the case of the equal-mass binaries, two neutron stars are tidally deformed in a noticeable manner only just before the onset of the merger (see Figs. 4 and 5). If the total mass is not large enough to form a black hole in the
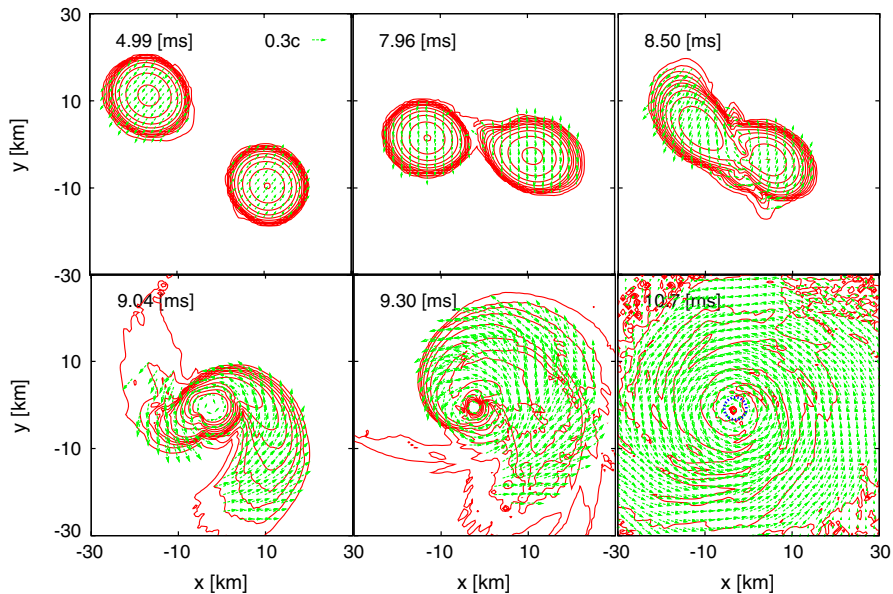

FIG. 6 (color online). The same as Fig. 5 but for run APR1316H.

dynamical time scale after the onset of the merger, a hypermassive neutron star of nonaxisymmetric structure is formed in the central region. In this case, spiral arms are formed in the outer region (see Fig. 4), and subsequently, they wind around the formed hypermassive neutron star, generating shocks in its outer region. Because of angular momentum dissipation by gravitational radiation, hydrodynamic interaction, and the hydrodynamic transport process of angular momentum, the density and specific angular momentum of the hypermassive neutron star are redistributed during the subsequent evolution and eventually it relaxes to a moderately ellipsoidal configuration. Here, the ellipticity remains because it is rapidly rotating and also the EOS is stiff enough as mentioned in Refs. [17,22]. As a result, the hypermassive neutron star emits gravitational waves subsequently, and it secularly evolves due to gravitational radiation reaction.

For the case when the total mass is large enough, the merged object collapses to a black hole in the dynamical time scale after the onset of the merger (see Fig. 5). In the equal-mass case, nearly all the material are swallowed by the black hole in ~ 1 ms. The resulting final outcome is a black hole surrounded by a tiny disk of mass $<10^{-3} M_\odot$.

In the unequal-mass case, the less massive neutron star is tidally deformed ~ 1 orbit before the onset of the merger (see the second panel of Fig. 6). Then, mass shedding occurs, and as a result, the material of the less massive neutron star accrete onto the massive companion. During the merger, it is highly tidally deformed, and thus, an efficient angular momentum transport occurs. Because of this, the material in the outer region of the less massive neutron star spread outward to form a spiral arm. This process helps formation of accretion disks around the formed black hole. The disk will survive for a time scale

much longer than the dynamical time scale as shown in Sec. IV B.

Figure 7 displays the density contour curves for the rest-mass density and the local velocity field on the $x = 0$ plane for runs APR1414H, APR145145H, APR1316H, and APR135165H. These also show that (i) a hypermassive neutron star of ellipsoidal shape is the outcome for model APR1414 [panel (a)], (ii) a black hole with tiny surrounding material is the outcome for model APR145145 [panel (b)], and (iii) a black hole surrounded by disks is the outcome for models APR1316 and APR135165 [panels (c) and (d)].

All these features are qualitatively the same as those reported in Ref. [17]. However, in the previous work, we employed initial conditions for which the initial separation is much smaller than that in the present work, as $m_0 \Omega_0 \sim 0.05$ where Ω_0 denotes initial orbital angular velocity. In the present work, $m_0 \Omega_0 \approx 0.027$, and this modification changes the results quantitatively. Furthermore, we performed the simulations for different total masses, and this leads to a new quantitative finding. In the remaining part of this subsection, we summarize the updated results.

As reported in the previous works [17,22], the final outcome formed after the merger (a black hole or neutron star) is primarily determined by a relation between the initial total mass m_0 and the threshold mass M_{thr} and by the mass ratio of the binary for a given EOS: The binary neutron stars of $m_0 > M_{thr}$ collapse to a black hole after the onset of the merger in the dynamical time scale ~ 1 ms. On the other hand, a hypermassive neutron star is formed for $m_0 < M_{thr}$, at least for a time much longer than the dynamical time scale. The threshold mass depends weakly on the mass ratio of the binary neutron stars.
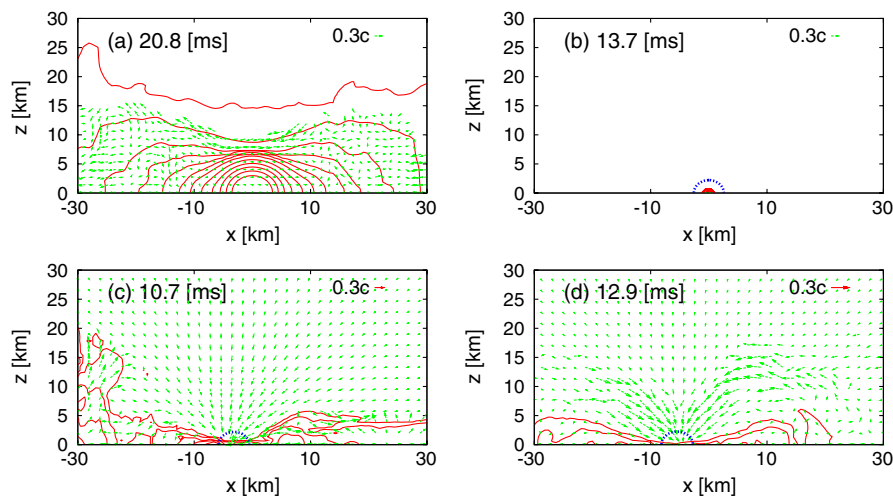

FIG. 7 (color online). Snapshots of the density contour curves for ρ and velocity field (v^y, v^z) on the $x = 0$ plane for runs (a) APR1414H, (b) APR145145H, (c) APR1316H, and (d) APR135165H. The time shown in the upper-left side denotes the elapsed time from the beginning of the simulation. The short-dashed half circles on the equatorial plane denotes the location of the apparent horizon.

The threshold mass, M_{thr}, depends strongly on the EOSs (on the stiffness of the EOS), and stiffer EOSs give larger values of M_{thr}. We reported in the previous work that for the APR EOS, $2.8M_\odot < M_{thr} < 3.0M_\odot$. In the present work, we find that the value of M_{thr} is in a narrower range between $2.8M_\odot$ and $2.9M_\odot$ via the study for models APR1414, APR145145, and APR1316. (Note that for models APR1414, APR145145, and APR1515, $m_0 = 2.8M_\odot$, $2.9M_\odot$, and $3.0M_\odot$, respectively.)

In the previous paper [17], we reported that the disk mass around the black hole is $\sim 4 \times 10^{-4}M_\odot$ for the equal-mass binary neutron star of total mass $m_0 = 3M_\odot$ and $\sim 0.003M_\odot$ for the binary neutron star of mass 1.35 and $1.65M_\odot$. We find that the mass of the disk at $t - t_{AH} = 3$ ms is $\approx 7 \times 10^{-5}M_\odot$ for model APR1515H and $\approx 6 \times 10^{-3}M_\odot$ for model APR135165 (see Fig. 9). Here, t_{AH} is the time when the apparent horizon (AH) is first formed. Thus, the disk mass is corrected by a factor of several, although the order of magnitude does not change. Also, we did not clarify the dependence of the disk mass on the total mass m_0 in the previous work. For model APR1316, we find that the disk mass at $t - t_{AH} = 3$ ms is $2.4 \times 10^{-2}M_\odot$, and thus, the disk mass depends strongly on the total mass of the system. More details about the merger process, final outcome, and disk mass will be discussed in subsequent subsections for each model separately.

1. APR1414

The total mass of this model is slightly smaller than the threshold mass, i.e., $m_0 < M_{thr}$, and hence, a compact hypermassive neutron star is formed. Because the total mass is close to M_{thr} in this model, the merged object first becomes very compact; e.g., α_{min} and ρ_{max} reach ~ 0.2 and $\sim 2 \times 10^{15}$ g/cm^3 soon after the first contact [see Fig. 3(a)]. Hence, the self-gravity is only slightly insufficient for inducing collapse to a black hole. The merged object subsequently bounces back to become an oscillating hypermassive neutron star. The quasiradial oscillation is repeated several times (see Fig. 3), and then the oscillation is damped due to shock dissipation and the hypermassive neutron star relaxes to a quasisteady ellipsoidal configuration [17], as found from the last panel of Figs. 4 and 7(a). These figures show that the axial ratio of the two major axes on the equatorial plane is ~ 0.9, and that of the polar coordinate radius r_p to the equatorial one r_e is $r_p/r_e \sim 0.7$. Thus, the ellipticity is not negligible. Such high ellipticity seems to reflect the fact that the hypermassive neutron star is rapidly rotating [70].

Figure 8(a) plots the angular velocity profile of the hypermassive neutron star in the late phase along the x and y axes. This shows that the hypermassive neutron star rotates rapidly and differentially. In the central region, the rotational period is ~ 0.5 ms, comparable to the dynamical time scale. This implies that centrifugal force around the central region plays an important role for supporting self-gravity. Note that the mass of the hypermassive neutron star is $\approx 30\%$ larger than the maximum allowed mass of spherical neutron stars of the APR EOS (which is $\approx 2.2M_\odot$), and hence, in the absence of rotation, the hypermassive neutron star would collapse to a black hole. Thus, the rapid rotation near the central region seems to be an essential agent for supporting its strong self-gravity. (We note that thermal energy generated by shock heating during the merger phase in part plays a role for supporting the self-gravity; see the discussion below.)

As we will discuss in Sec. IV C, the hypermassive neutron star continuously emits gravitational waves and loses angular momentum because it has a nonaxisymmetric shape and rapid rotation. This indicates that it may eventually collapse to a black hole after a substantial fraction of the angular momentum is dissipated from the central region. The lifetime of the hypermassive neutron star may be estimated by calculating the time scale for the angular momentum loss due to the gravitational-wave emission. At the end of the simulation ($t \sim 20$ ms), the angular momentum and its dissipation rate are $J \sim 0.74J_0 \sim 4.9 \times 10^{49}$ g cm^2 s^{-1} and $dJ/dt \sim 6.7 \times 10^{49}$ g cm^2 s^{-2}, respectively. The lifetime of the hypermassive neutron star may be estimated by $J/(dJ/dt) \sim 700$ ms. dJ/dt (namely the amplitude of gravitational waves) gradually decreases with time, and hence, this time scale should be regarded as the shortest one. However, the decreased time scale of dJ/dt is not as short as the dynamical time scale, and thus, the estimated time scale is likely to be correct within the factor of 2–3. If this estimation is correct, the hypermassive neutron star would collapse to a black hole in a few seconds (but see the discussion below for other possibilities). Other physical processes, which are not taken into account in this work, could also contribute to dissipating and/or transporting angular momentum: Because the hypermassive neutron star rotates differentially as shown in Fig. 8, magnetic fields might be amplified by the magneto-rotational instability and/or magnetic winding [71–73]. As a result, angular momentum may be transported efficiently, leading the hypermassive neutron star to collapse to a black hole. If the time scale for the magnetic processes is shorter than the emission time scale of gravitational waves, they would be the main agent for inducing gravitational collapse to a black hole.

As discussed above, the hypermassive neutron star eventually collapses to a black hole in any scenario. Because the hypermassive neutron star has a spread envelope (see the last three panels of Fig. 3), the final black hole formed after the gravitational collapse may be surrounded by an accretion disk. To qualitatively estimate the outcome, we generate Fig. 8(b) which shows the evolution of the mass spectrum as a function of the specific angular momentum $M_*(j)$ where $j = hu_\varphi$ is the specific angular momentum of each fluid element. Here, $M_*(j)$ is defined as an integrated baryon mass of fluid elements with $j > j'$;
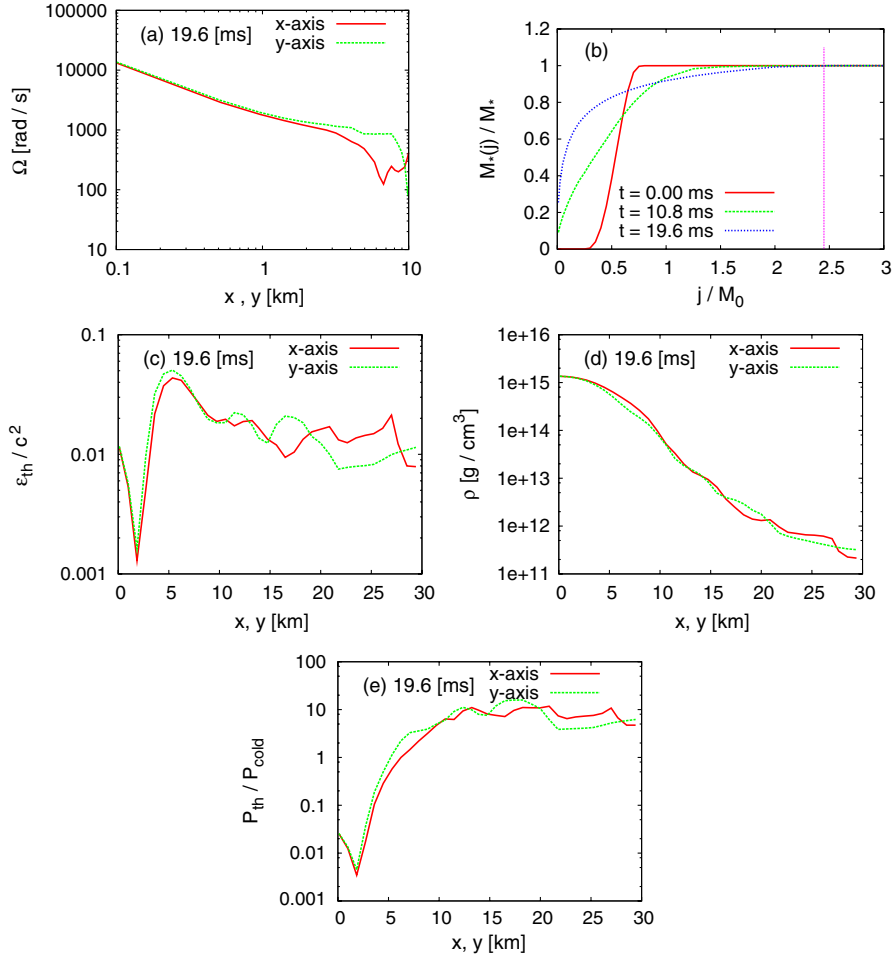
FIG. 8 (color online).   Various quantities of hypermassive neutron star formed for run APR1414H. (a) Profiles of angular velocity along x and y axes at $t = 19.6$ ms; (b) Mass spectrum as a function of specific angular momentum at the selected time slices. The vertical dotted line denotes the specific angular momentum at the innermost stable circular orbit around the black hole of mass $0.97M_0$ and spin $a = 0.77$; (c)–(e) Specific thermal energy, rest-mass density, and ratio of the thermal pressure to the nuclear-matter pressure, $P_{\rm th}/P_{\rm cold}$, along x and y axes at $t = 19.6$ ms.

$$M_*(j) = \int_{j' < j} \rho_*(x')d^3x'. \qquad (4.1)$$

Figure 8(b) shows that the value of j for most of the fluid elements is smaller than $2M_0$ for $t \lesssim 20$ ms. However, the fraction of the mass element of $j \gtrsim M_0$ increases with time. This indicates that angular momentum is transported outward due to nonaxisymmetric hydrodynamic interaction.

The ADM mass and angular momentum at the end of the simulation ($t \approx 20$ ms) are $\approx 0.97M_0$ and $0.74J_0$, respectively, and thus, the nondimensional spin parameter of the system is ~ 0.77. Then, assume that the final mass and spin of the black hole (BH) would be $M_{\rm BH} \sim 0.97M_0$ and $a \sim 0.77$. Specific angular momentum at the innermost stable circular orbit (ISCO), $j_{\rm ISCO}$, of such a rotating black hole is given by $\approx 2.45M_0$ (e.g., Ref. [57]). This suggests that a fluid element of $j \gtrsim 2.45M_0$ would be able to form a disk surrounding the black hole. Figure 8(b) shows that any

mass element does not have specific angular momentum large enough to form the disk. However, the profile of the mass spectrum quickly changes with time by the hydrodynamic angular momentum transport, as mentioned above. The estimated lifetime of the hypermassive neutron star is a few seconds, and much longer than 20 ms. This suggests that a substantial fraction of the fluid elements may form an accretion disk.

Finally, we touch on thermal effects on the evolution of the hypermassive neutron star. Because shocks are generated during the merger and in the subsequent dynamical phase, the hypermassive neutron star is heated up and as a result, the specific thermal energy, $\varepsilon_{\rm th}$, becomes nonzero. To clarify the role of the generated thermal energy, we plot the profiles of $\varepsilon_{\rm th}$, ρ, and $P_{\rm th}/P_{\rm cold}$ along the x and y axes in Figs. 8(c)–8(e). Figure 8(c) shows that the value of $\varepsilon_{\rm th}/c^2$ is 0.002–0.05 for a region of $\rho \gtrsim \rho_{\rm nuc} \approx 2 \times 10^{14}$ g/cm^3, where $\rho_{\rm nuc}$ denotes the nuclear density, and for the region of subnuclear density, it is 0.01–0.02. Assuming that the
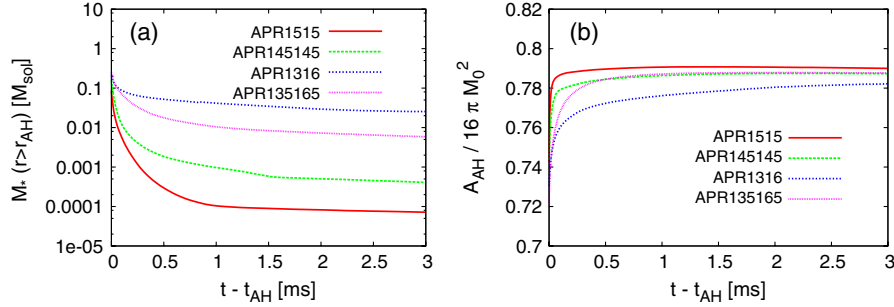
FIG. 9 (color online).   The evolution of (a) the rest-mass of disks surrounding black holes and (b) the evolution of the area of apparent horizons for runs APR145145H, APR1515H, APR1316H, and APR135165H. t_{AH} denotes the time at which the apparent horizon is formed.

matter field is composed of neutron gas and thermal radiation, the temperature of the region with $\rho \gtrsim 10^{11}$ g/cm^3 (above which the optical depth for neutrino transport would be larger than unity and the cooling due to the neutrino emission would not be efficient) is approximately calculated to give a high temperature as $7.2 \times 10^{10}(\varepsilon_{th}/0.01c^2)$ K. Nevertheless, the thermal pressure P_{th} in the central region of $\rho \gtrsim 10^{15}$ g/cm^3 is only $\sim 1\%$–2% of P_{cold} as shown in Fig. 8(e), and hence, the thermal pressure plays a minor role for supporting the self-gravity in the central region. This indicates that centrifugal force plays a more important role for supporting the self-gravity of the hypermassive neutron star in its early evolution phase. By contrast, for a region of $\rho \lesssim \rho_{nuc}$, the thermal pressure is larger than P_{cold}. Namely, the effect of the thermal energy plays an important role for determining the profile in the envelope of the hypermassive neutron star.

Although the ratio P_{th}/P_{cold} is small in the central region, it is not a negligible value and the thermal pressure seems to contribute in part to supporting the self-gravity. This suggests that even after dissipation and/or transportation of angular momentum via gravitational radiation or magnetic-field effects, the hypermassive neutron star of relatively small mass may not collapse to a black hole because of the presence of the thermal energy. If so, the collapse will set in after the thermal energy is dissipated via neutrino cooling. The cooling time scale by neutrino emission from the central region of the hypermassive neutron star is likely to be of the order 10–100 s (e.g., Chaps. 11 and 18 of Ref. [57]), and thus, the lifetime of the hypermassive neutron star of relatively low mass may be rather long.

In all the above scenarios, the hypermassive neutron star eventually collapses to a black hole after a substantial fraction of angular momentum is dissipated. This indicates that the resulting black hole will not be rotating as rapidly as the black holes promptly formed after the onset of the merger (cf. Sec. IV B).

For the envelop of the hypermassive neutron star, $\varepsilon_{th} \sim$ 0.01–0.02 and the temperature of this region is high, $\sim 10^{11}$ K. Because of its high temperature and relatively

low density, such a region is subject to a large amount of thermal neutrino emission. In particular, for the region of $\rho \lesssim 10^{11}$ g/cm^3, neutrinos are not trapped by the matter but escape freely, so cooling will proceed rapidly. Thus, the thermal energy decreases on a time scale, shorter than the dynamical time scale, until the cooling time scale becomes as long as the dynamical one. This point should be explored in the future, incorporating finite-temperature EOSs and the neutrino emission, although such work is beyond the scope of this paper.

2. APR145145, APR1515

In these equal-mass massive models, a black-hole is formed after the onset of merger in dynamical time scale ~ 1 ms, and most of the material falls into the black-hole (e.g., the last two panels of Fig. 5). Figure 9(a) plots the evolution of $M_{r>r_{AH}}$, which denotes the rest mass of the baryon located outside the apparent horizon, for runs APR145145H and APR1515H. Here, $M_{r>r_{AH}}$ is defined by

$$M_{r>r_{AH}} \equiv \int_{r>r_{AH}} \rho_* d^3x, \qquad (4.2)$$

where $r_{AH}[= r_{AH}(\theta, \varphi)]$ denotes the radius of the apparent horizon.

This figure shows that more than 99% of the fluid elements are swallowed by the black hole within ~ 0.1 ms after the formation of the apparent horizon. The primary reason for this rapid infalling is that the specific angular momentum j_{ini} at the onset of the merger is too small for all the fluid elements: The maximum value of the specific angular momentum at the onset of merger, j_{max}, is about $1.25M_0$ for both of the models. As discussed in Sec. IV B, the final value of the black hole spin is estimated to be ≈ 0.8 for both the models. This predicts that the specific angular momentum at ISCO around the formed black hole is $\approx 2.4M_0$, which is much larger than j_{max}. Moreover, the angular momentum transport works inefficiently because of the equal-mass symmetry (see Fig. 5) and also the specific angular momentum decreases due to the gravitational-wave emission during the merger. All of

these facts indicate that formation of massive disks surrounding the black hole is unlikely.

The disk mass for model APR1515 is smaller than that for model APR145145. The likely reason for this is that the object formed just after the onset of the merger for model APR1515 is more compact than that for model APR145145. As a result, (i) the dynamical time scale becomes shorter and the time duration for which the angular momentum transport works does as well; (ii) dissipation of angular momentum by gravitational waves is larger and disk formation becomes less likely. This dependence of the disk mass on the total mass is also found in the merger of unequal-mass binary neutron stars (see Sec. IV A 3).

Accretion time scale for the disk and increase time scale of the area of the apparent horizon are much longer than the dynamical time scale (i.e., rotational time scale of the disk) for $t - t_{AH} \gtrsim 1.5$ ms, as shown in Fig. 9(b). Therefore, the final state formed for these models is a rapidly rotating black hole surrounded by a quasisteady disk of tiny mass [see Fig. 7(b)].

We compare the result for the disk mass in the present and previous simulations for model APR1515. In Ref. [17], we reported that the final disk mass is $\sim 4 \times 10^{-4} M_\odot$, whereas it is $\sim 7 \times 10^{-5} M_\odot$ for the present work. This difference seems to originate simply from the fact that we evaluated the disk mass soon after its formation ($t - t_{AH} = 0.5$ ms) in Ref. [17]; i.e., the disk mass is evaluated before the disk relaxes to a quasisteady state. In the present work, we can evaluate it at $t - t_{AH} = 3.0$ ms, at which the disk is in a quasisteady state, because we employ the moving-puncture method which enables us to perform a long-term simulation even after black hole formation.

3. APR1316, APR135165

As shown in Ref. [17] and in Fig. 5, the less massive neutron star is significantly tidally deformed in the final inspiral phase of unequal-mass binary neutron stars, and then, the merger occurs. At the onset of the merger, the less massive star is highly elongated and hence its outer part subsequently forms a large spiral arm. The merger in the central part simultaneously proceeds and, for the case that

$m_0 > M_{thr}$, a black hole is formed around the center in a dynamical time scale ~ 1 ms. One interesting feature in the early stage of the merger (before gravitational collapse to a black hole) is that material in the inner part of the less massive star slips through the surface of the companion neutron star and forms a small spiral arm. As a result, two asymmetric spiral arms are formed around the central object which subsequently collapses to a black hole (see the fourth panel of Fig. 6). Because of the nonaxisymmetric structure, the angular momentum is transported outwards in the spiral arms. Because the rotation velocity of the small spiral arm around the central object is faster than that of the large spiral arm, they collide within one orbit. As a result, shocks are formed and the material in the spiral arms is heated up. In this mechanism, kinetic energy of the material is converted into thermal energy, and then a part of the fluid elements, which lose the kinetic energy, are swallowed by the black hole (see Fig. 9). The fluid elements which escape from falling into the black hole eventually form a disk around the black hole. All of these features were already found in Ref. [17], but in the previous work, the simulation was not able to continue for a time long enough to determine the final state because the simulation crashed before a quasisteady state was reached. As Fig. 9(b) indicates, the present simulations, by contrast, have been done until the final state (composed of a black hole and quasisteady accretion disk) is reached, and the conclusive statement becomes possible.

Figures 7(c) and 7(d) also show that the final outcomes for models APR1316 and APR135165 are a rotating black hole surrounded by a disk. The disk mass for runs APR1316H and APR135165H evaluated at $t - t_{AH} = 3.0$ ms is about 2.4×10^{-2} and $6.4 \times 10^{-3} M_\odot$, respectively, [see Fig. 9(a) and Table III]. The likely reason for this significant difference is that for the less massive binary neutron star, the system at the onset of merger is less compact and has a longer dynamical time scale for transporting angular momentum outward more efficiently, as already mentioned in Sec. IV A 2.

The disk mass computed for three grid resolutions are described in Table III. We find that the disk mass does not systematically converge and the magnitude of the error
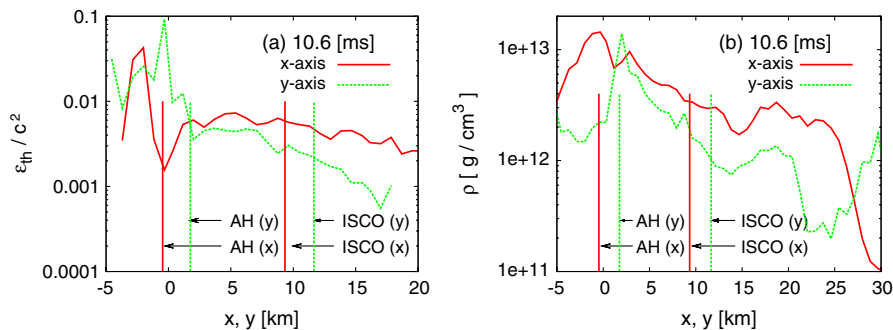

FIG. 10 (color online). Profiles of (a) specific thermal energy and (b) density for run APR1316H. The vertical solid (dashed) lines denote the location of the AH (ISCO).

TABLE III. Key numerical results for models APR145145, APR1515, APR1316, and APR135165. ΔE, ΔJ, $M_{r>r_{AH}}$, $\hat{A}_{AH}$, C_p, C_e, and f_{QNM} denote energy and angular momentum carried by gravitational waves, rest mass of the material located outside the apparent horizon, area of the apparent horizon in units of $16\pi M_{BH,f}^2$, polar and equatorial circumferential radii of the apparent horizon, and quasinormal mode frequency, respectively. $M_{r>r_{AH}}$ and f_{QNM} are given in units of M_0 and kHz, respectively. f_{QNM} is derived from Eq. (4.11) using $M_{BH,f}$ and a_{f2}. For all the models, results for three grid resolutions are presented. All the quantities are evaluated when we stopped the simulations.

Model	$\Delta E/M_0$	$\Delta J/J_0$	$M_{r>r_{AH}}$	$M_{BH,f}/M_0$	$\hat{A}_{AH}$	$C_e/4\pi M_0$	C_p/C_e	a_{f1}	a_{f2}	a_{f3}	f_{QNM}
APR145145L	1.15%	16.7%	0.025%	0.988	0.8208	0.9880	0.8628	0.84	0.77	0.77	6.67
APR145145M	1.16%	17.4%	0.010%	0.987	0.8123	0.9863	0.8585	0.83	0.78	0.78	6.76
APR145145H	1.19%	17.9%	0.017%	0.988	0.8060	0.9843	0.8569	0.82	0.79	0.78	6.81
APR1515L	1.19%	16.9%	0.004%	0.988	0.8092	0.9864	0.8576	0.84	0.79	0.78	6.56
APR1515M	1.21%	18.0%	0.002%	0.988	0.8126	0.9862	0.8570	0.83	0.78	0.78	6.53
APR1515H	1.24%	18.9%	0.004%	0.987	0.8101	0.9867	0.8569	0.81	0.78	0.78	6.56
APR1316L	1.11%	15.6%	0.72%	0.982	0.8098	0.9730	0.8627	0.83	0.78	0.77	6.76
APR1316M	1.17%	16.9%	0.74%	0.981	0.8181	0.9750	0.8662	0.83	0.77	0.76	6.70
APR1316H	1.18%	17.5%	0.85%	0.980	0.8156	0.9752	0.8633	0.83	0.78	0.77	6.71
APR135165L	1.10%	15.8%	0.23%	0.987	0.8101	0.9804	0.8643	0.83	0.78	0.76	6.53
APR135165M	1.15%	17.1%	0.14%	0.987	0.8111	0.9801	0.8615	0.82	0.78	0.77	6.52
APR135165H	1.17%	17.8%	0.21%	0.986	0.8102	0.9818	0.8607	0.81	0.78	0.77	6.53

seems to be by $\sim 50\%$. The likely reason for the slow convergence is that the grid resolution in the outer domain (where the fluid elements spread) is not systematically improved as the grid resolution in the inner domain is improved and the disk mass depends sensitively on the spurious numerical transport process of angular momentum (see, e.g., Ref. [74] for a discussion about slow convergence of disk mass in the black hole-neutron star merger). However, all the numerical results are derived in a fairly narrow range irrespective of the grid resolution, and the order of magnitude of the disk mass does not depend on the grid resolution.

In the previous paper [17], the merger of the unequal-mass binary neutron stars collapsing to a black hole was studied only for $m_0 = 3M_\odot$. We reported that for the mass ratio $Q_M \gtrsim 0.8$, the rest mass of the disk surrounding the black hole was likely to be smaller than $0.01M_\odot$. The present results indicate that the disk mass depends sensitively on the total mass of the system, and even for the case that the mass ratio is not much smaller than unity, a system composed of a black hole and massive disk may be an outcome after the merger, if the total mass is close to M_{thr}.

For model APR1316, the disk mass is larger than $0.01M_\odot$ with a high maximum rest-mass density $\sim 10^{12}$ g/cm^3 in its inner region, as shown in Fig. 10. Also, the thermal energy is generated by shock heating, resulting in a high specific internal energy, $\varepsilon/c^2 \sim 0.01$ which implies a high matter temperature as $7.2 \times 10^{10}(\varepsilon_{th}/0.01c^2)$ K (see Fig. 10). All these properties are favorable for producing a large amount of high-energy neutrinos, from which electron-positron pairs and γ rays may be generated [14]. Thus, the final outcome is a candidate for the central engine of short GRBs.

B. Black hole mass and spin

As mentioned in the previous subsections, the final outcomes after the merger for models APR145145, APR1515, APR1316, and APR135165 are a rotating black hole. Here we determine the black hole mass, $M_{BH,f}$, and spin, a_f, using the same methods as those used in Refs. [25,34].

There are at least two methods for (approximately) estimating the black-hole mass and three methods for estimating the black-hole spin. In the first method for estimating the black-hole mass and spin, we use the conservation laws. The energy conservation law is approximately written as

$$M_{BH,f} = M_0 - M_{r>r_{AH}} - \Delta E, \qquad (4.3)$$

where M_0 is the initial ADM mass of the system. In Eq. (4.3), we neglect the binding energy between the black-hole and surrounding matter, but it is likely to be at most 10% of $M_{r>r_{AH}}$ and thus a minor correction.

Conservation law of angular momentum is approximately written as

$$J_{BH,f} = J_0 - J_{r>r_{AH}} - \Delta J, \qquad (4.4)$$

where $J_{BH,f}$ is the angular momentum of the black hole and J_0 is total angular momentum at $t = 0$. $J_{r>r_{AH}}$ approximately denotes angular momentum of the material located outside the apparent horizon which is defined by

$$J_{r>r_{AH}} \equiv \int_{r>r_{AH}} \rho_* h u_\varphi d^3 x, \qquad (4.5)$$

where u_φ is the φ component of the four velocity. We note that $J_{r>r_{AH}}$ is strictly equal to the angular momentum of material only for stationary axisymmetric systems. Thus,

this should be adopted only for the case that the system approximately relaxes to a stationary axisymmetric spacetime.

From $M_{BH,f}$ and $J_{BH,f}$, a nondimensional spin parameter is defined by

$$a = \frac{J_{BH,f}}{M_{BH,f}^2}. \qquad (4.6)$$

Hereafter, we refer to this spin as a_{f1}.

In the second method, the mass and spin of the black holes are determined using geometrical properties of apparent horizon. When the system relaxes to a quasisteady state, the black hole mass may be approximately estimated from equatorial circumferential length C_e of the apparent horizon, because $C_e/4\pi$ is equal to $M_{BH,f}$ for Kerr black holes. This value also gives an approximate value of the black hole mass even in the presence of surrounding torus [75].

Next, we assume that area of apparent horizon, A_{AH}, obeys the same relation as that of Kerr black holes;

$$\hat{A}_{AH} \equiv \frac{\pi A_{AH}}{C_e^2} = \frac{1 + \sqrt{1 - a^2}}{2}. \qquad (4.7)$$

Then, from $\hat{A}_{AH}$ and C_e, a black hole spin may be estimated. Hereafter, we refer to this spin as a_{f2}. Note that this method should be used only in the case that the system relaxes to a quasisteady state, because Eq. (4.7) holds only for such spacetime.

A black hole spin is also estimated from polar and equatorial circumferential radii of apparent horizon, C_p and C_e. For Kerr black holes, the ratio C_p/C_e is given by a known function composed only of the black hole spin as

$$\frac{C_p}{C_e} = \frac{\sqrt{2\hat{r}_+}}{\pi} \int_0^{\pi/2} \sqrt{1 - \frac{a_f^2}{2\hat{r}_+} \sin^2\theta} d\theta, \qquad (4.8)$$

where $\hat{r}_+ = 1 + \sqrt{1 - a^2}$. The black hole spin determined from C_p/C_e is referred to as a_{f3} in the following.

All the results for the black hole mass and spin are summarized in Table III. We find that $M_{BH,f}$ and $C_e/4\pi$ agree within 0.5% error for all the models. This indicates that both quantities at least approximately denote the black hole mass and that we obtain the black hole mass within ~0.5% error.

The spin parameters a_{f2} and a_{f3} agree within 0.01 for all of the models. However, the spin parameters a_{f1} do not agree well with a_{f2} and a_{f3}. The typical size of the difference is 0.06–0.07, 0.05–0.07, and 0.04–0.06 for low-, medium-, and high-grid resolutions, respectively. Because the magnitude of the difference decreases systematically with the improvement of the grid resolution, this discrepancy originates primarily from numerical error associated with the finite grid resolution. As discussed in Ref. [25], poor grid resolution enhances spurious dissipa-

tion of angular momentum and shortens the time duration of the inspiral phase. This leads to the underestimation of ΔJ. Indeed, the time duration of the inspiral phase and ΔJ increase with improvement of the grid resolution, and as a result, the value of a_{f1} systematically decreases (see Table III). By contrast, C_p/C_e and $\hat{A}_{AH}$ depend weakly on the grid resolution, and so do a_{f2} and a_{f3}. This suggests that the convergent value of the black hole spin is close to a_{f2} and a_{f3}, and therefore, we conclude that for all the models, the black hole spin is $a_f \approx 0.78 \pm 0.02$.

In the merger of equal mass, nonspinning binary black holes, a_f is ≈ 0.69 [32,47], which is by about 0.1 smaller than that for the merger of binary neutron stars. This difference arises primarily from the magnitude of dJ/dt in the final phase of coalescence. In the merger of binary black holes, a significant fraction of angular momentum is dissipated by gravitational radiation during the last inspiral, merger, and ringdown phases, because a highly nonaxisymmetric state is accompanied by a highly compact state from the last orbit due to the high compactness of the black holes. By contrast, compactness of the neutron stars is a factor of ~5–7 smaller, and as a result, such a highly nonaxisymmetric and compact state is not achieved for the binary neutron stars. Indeed, the angular momentum loss rate by gravitational waves during the last phases is much smaller than that of the binary black holes.

Finally, we comment on the dependence of the black hole mass and spin on the approaching velocity. As discussed in Sec. IIIC, our prescription of the approaching velocity can reduce the initial eccentricity. By comparing the result for run APR1515L with/without approaching velocity, we find that the spin and mass of the final state of the black hole are insensitive to the initial orbital eccentricity.

C. Gravitational waves

1. General feature and convergence

Figure 11 plots gravitational waveforms as a function of a retarded time for runs APR1414H, APR1515H, APR1316H, and APR135165H. Here, the retarded time is defined by

$$t_{ret} \equiv t - D - 2M_0 \ln(D/M_0), \qquad (4.9)$$

where D is the distance between the source and an observer. For comparison, inspiral waveforms calculated by the Taylor T4 formula are plotted together by the dashed curves.

For the case that a hypermassive neutron star is the outcome after the merger (for model APR1414), gravitational waves are composed of the inspiral, merger, and quasiperiodic waveforms. Here, the merger waveform denotes short-term burst-type waves emitted after the inspiral phase and before the hypermassive neutron star relaxes to a quasisteady state. The quasiperiodic waveforms seen for
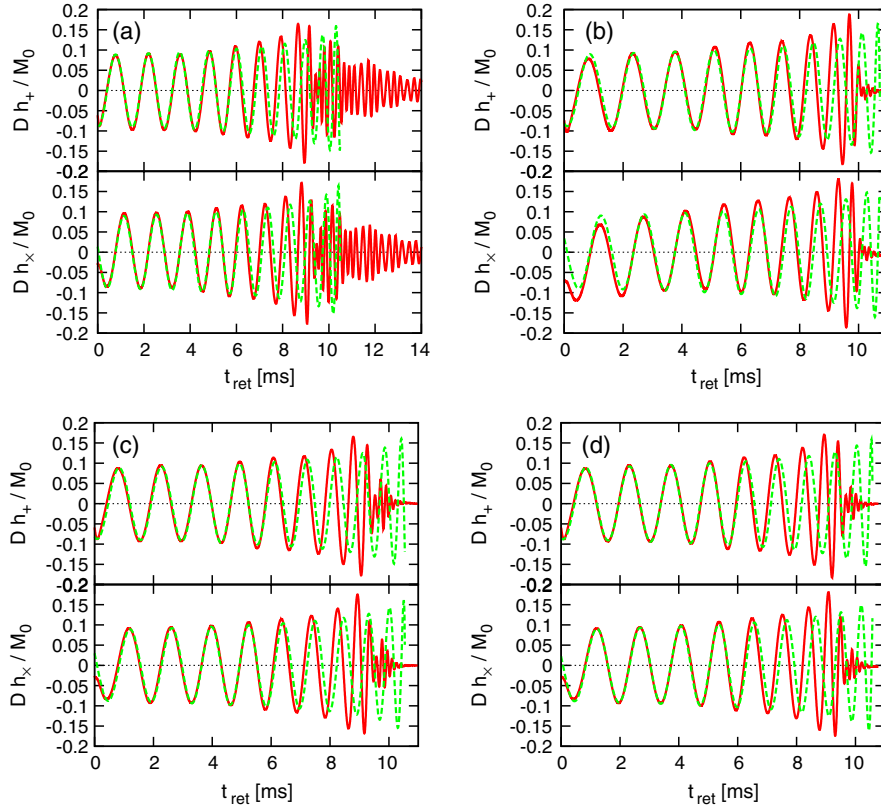
FIG. 11 (color online). $h_{+,\times}$ for runs (a) APR1414H, (b) APR1515H, (c) APR1316H, and (d) APR135165H. In each panel, the top (bottom) one is $h_+(h_\times)$, and the solid and dashed curves denote the waveforms calculated by the simulation and Taylor T4 formula, respectively.

model APR1414 are emitted by rapidly rotational motion of the ellipsoidal hypermassive neutron star and their amplitude is comparable to that of the late inspiral phase. Gravitational waves of nearly identical frequency ($f \sim$ 3.8 kHz for this model) are emitted for many cycles in the quasiperiodic phase, because the dissipation time scale of the rotational kinetic energy by gravitational radiation reaction is much longer than the rotational time scale. Consequently, the effective (time-integrated) amplitude of gravitational waves is much larger than that for the late inspiral phase of frequency $f \sim 1$ kHz (cf. Sec. IV C 4). This property is essentially the same as that found in our previous works [17,22].

For the case that a black hole is formed in a dynamical time scale after the onset of the merger (for models APR145145, APR1515, APR1316, and APR135165), gravitational waves are composed of the inspiral, merger, and ringdown waveforms. Because a rotating black hole in a quasisteady state is the final outcome after the merger, the ringdown waveform is characterized by the fundamental quasinormal mode of the formed black hole. This is a universal qualitative feature that holds irrespective of the total mass and mass ratio of the binary neutron stars, but the amplitude and characteristic frequency of gravitational waves depend strongly on these parameters (see

Sec. IV C 3). All of these properties were not clarified in the previous work [17]. The merger waveform denotes short-term burst-type waves emitted after the inspiral phase and before the ringdown phase. The frequency of gravitational waves in the merger phase is slightly lower than the frequency of the black hole quasinormal mode, but the amplitude is much larger than that of the ringdown waveform. The frequency and amplitude of the merger waveform are seen in the Fourier space in a better manner (see the discussion in Secs. IV C 3 and IV C 4).

2. Inspiral gravitational waves

Figure 11 shows that the inspiral waveforms are fitted in part well with those derived by the Taylor T4 formula. For comparing the frequency of gravitational waves as a function of time, the orbital angular velocity derived from gravitational waves is plotted in Fig. 12 for models APR1414, APR1515, APR1316, and APR135165. Here, the angular velocity, Ω, is computed from Ψ_4 by

$$\Omega = \frac{|\Psi_4(l = m = 2)|}{2|\int dt \Psi_4(l = m = 2)|}. \tag{4.10}$$

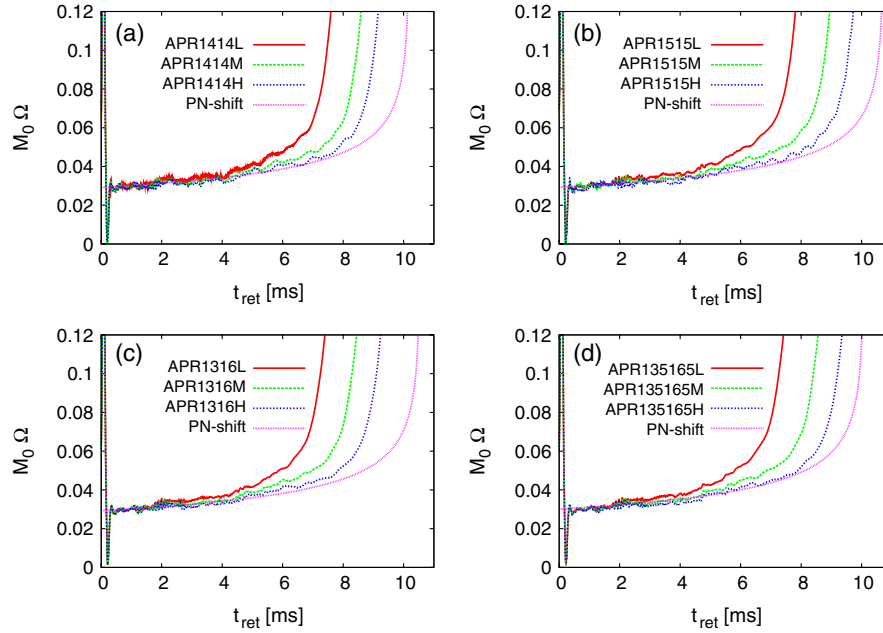In Fig. 12, the solid, dashed, short-dashed, and dotted curves are numerical results with three grid resolutions

FIG. 12 (color online). The evolution of the orbital angular velocity $M_0\Omega$ derived from Ψ_4 for models (a) APR1414, (b) APR1515, (c) APR1316, and (d) APR135165. The solid, dashed, short-dashed, and dotted curves denote the angular velocity derived by runs of different grid resolutions and Taylor T4 formula, respectively.

and results by the Taylor T4 formula, respectively. In comparison, the time axis for the results by the Taylor T4 formula is shifted according to the prescription described in Sec. II D.

Figure 12 shows that with the lowest-resolution run, the numerical results agree approximately with that of the Taylor T4 formula only for a short time (2 ms $\lesssim t_{\rm ret} \lesssim$ 4 ms). The time span, during which the numerical results are fitted well by the Taylor T4 formula, is longer for the better grid resolutions. Thus, disagreement of the numerical waveforms with those by the Taylor T4 formula is simply due to the fact that the grid resolution is insufficient. The more specific reason is that angular momentum is numerically dissipated more for the lower grid resolution, as mentioned in Sec. IV B. As a result, merger time (defined as the time when the merger sets in, and approximately equal to the time spent in the inspiral phase) is spuriously shortened and the number of the wave cycles in the inspiral phase is spuriously reduced, resulting in a disagreement of the orbital phase with the Taylor T4's result. These properties are observed in all the models (see also Fig. 13).

The numerical results for the angular velocity curve do not agree with the curve derived by the Taylor T4 formula even with the highest-resolution run. To clarify the reason for this disagreement, we generate Fig. 14, in which the results (a) for runs APR1515L and APR1515M and (b) for runs APR1316L and APR1316M are replotted by shifting the time axis to align the merger time for the results of three grid resolutions. Then, we also replot the result by the Taylor T4 formula so that it fits well with the overlapped

numerical results. This figure shows that the results of three grid resolutions approximately agree with each other and also with the result obtained by the Taylor T4 formula for 4 ms $\lesssim t_{\rm ret} \lesssim$ 8 ms, whereas for $t_{\rm ret} \gtrsim$ 8 ms three numerical results deviate from the result of the Taylor T4 formula. This suggests that (i) for the late inspiral phase (for 4 ms $\lesssim t_{\rm ret} \lesssim$ 10 ms in this figure), the numerical results are approximately convergent and reliable and (ii) the disagreement with the results by the Taylor T4 formula comes from a reason different from the numerical error. The most plausible reason is that for such a late inspiral phase, a finite size effect of neutron stars, which is not taken into account in the Taylor T4 formula, plays an important role for accelerating the inward motion [76] because tidal deformation of two neutron stars and its effect are not negligible for the last orbits.

In the binary BH system, the comparison of the PN and numerical-relativity waveforms have been extensively done, varying the PN order, changing the expression of the PN formula (e.g., Taylor T1, T4, and Et), and including spins of black holes [32,49,54,77,78]. The consensus is that the Taylor T4 formula is valid for $m_0\Omega \lesssim 0.1$. However, this is not the case for binary neutron stars because the finite size effect plays an important role for them, as mentioned above. We infer that the criterion will depend on the EOS of neutron stars, because it determines compactness of neutron stars and thus degree of tidal deformation. For proving this point more strictly, however, it is necessary to compute waveforms with a higher precision in which a sufficient convergence can be achieved. This is an issue left for the future.
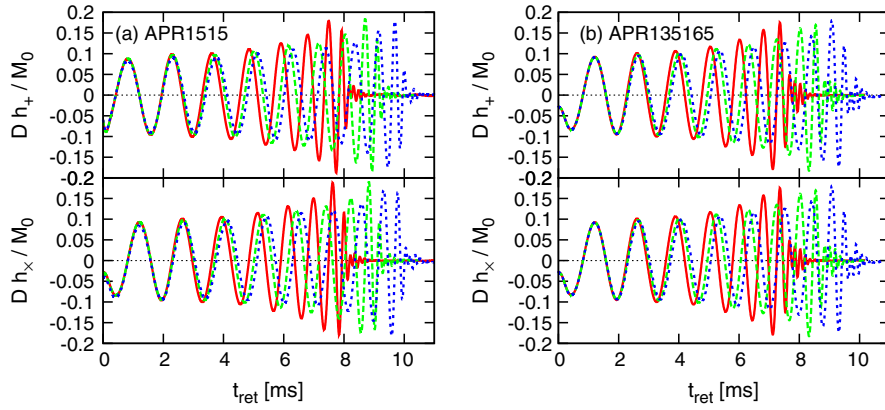
FIG. 13 (color online). The same as Fig. 11, but for models APR1515 and APR135165. In each panel, the solid, dashed, and short-dashed curves denote the results for low, medium, and high-resolution runs, respectively.

Before closing this subsection, we touch on the convergence of the inspiral waveforms. As mentioned above, the wave cycle is spuriously shorten for the lower grid-resolution simulations. Figure 15(a) plots the merger time as a function of Δx^2, where we define the merger time as the time when $M_0 \Omega$ reaches 0.12 (see Fig. 12). We find that the merger time converges approximately at second order. Comparing the merger time derived by the highest-resolution run with that derived by the extrapolated result, we find that the merger time is by ~ 2 ms underestimated irrespective of models. This suggests that ~ 2 wave cycles are spuriously lost: Figure 13(b) suggests that the wave cycles in an early phase of the numerical simulation seem to be lost. To derive more accurate gravitational waveforms for the inspiral phase, say, those with the error of half cycle, a higher grid resolution is required. For this purpose, the present simulation with unigrid domain is computationally expensive (although it is in principle possible to perform the simulation), and hence, an adaptive mesh refinement (AMR) algorithm would be required [25,26,79]. Because the purpose of this paper is not to derive highly precise inspiral gravitational waveforms but to qualitatively explore gravitational waves in the merger and subsequent phases, we do not pay attention to the inspiral waveforms in more detail.

3. Merger and ringdown gravitational waves

In contrast to the results for the inspiral waveforms, the numerical results for the merger and ringdown waveforms have a good convergence, and the grid resolution chosen in this work appears to be acceptable. Figure 15(b) plots Ψ_4 as a function of the retard time for runs APR1515L, APR1515M, and APR1515H. To focus on the ringdown waveforms in comparison among three runs, the time is shifted for runs APR1515L and APR1515M, to align the phase in the ringdown waveforms. This figure shows that the phase of the waveforms agrees well for 10 ms $\lesssim t_{\mathrm{ret}} \lesssim$ 11.5 ms. The amplitude of gravitational waves slightly disagree, but the error is at most $\sim 20\%$ for the lowest-resolution run and for the highest-resolution run, it appears to be less than 5% (note that this does not originate from the finite extraction radius as shown in Fig. 1). This indicates that the grid resolution for model APR1515H and resulting spurious short merger time do not seriously affect the merger and ringdown waveforms. This feature does not depend on the total mass or mass ratio of the model. Thus for a quantitative study of the merger and ringdown waveform, the highest grid resolution adopted in this paper is acceptable.

As mentioned in Sec. IV C 1, the waveforms in the ringdown phase are primarily characterized by the funda-
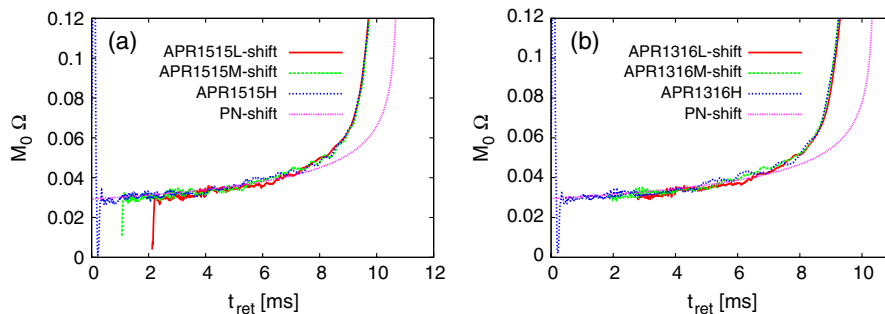

FIG. 14 (color online). (a) The same as Fig. 12(b) but the numerical results for runs APR1515L and APR1515M are plotted by shifting the time coordinates to align the merger time with run APR1515H. (b) The same as (b) but for model APR1316.
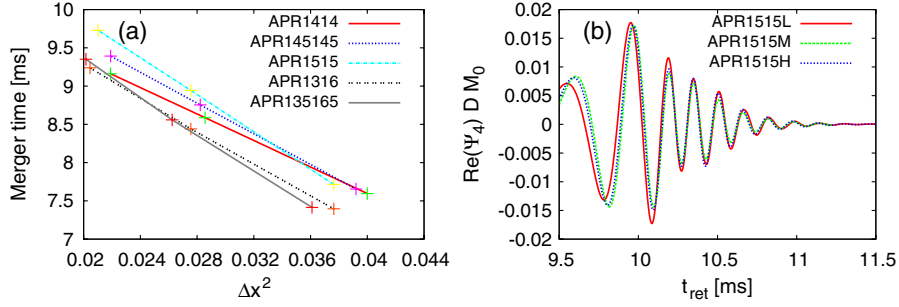
FIG. 15 (color online). (a) The numerical results for merger time as a function of Δx^2 for all the models and (b) Ψ_4 as a function of retarded time for runs APR1515L, APR1515M, and APR1515H. To align the phase, the time coordinates for runs APR1515L and APR1515M are shifted.

mental quasinormal mode (QNM) of the formed black holes for models APR145145, APR1515, APR1316, and APR135165. To clarify this fact, Fig. 16 plots Ψ_4 together with a fitting formula in the form

$$A e^{-t/t_d} \sin(2\pi f_{\mathrm{QNM}} t + \delta), \tag{4.11}$$

where A and δ are constants, and the frequency and damping time scale are predicted by a linear perturbation analysis as [80,81]

$$f_{\mathrm{QNM}} \approx 10.7\left(\frac{M_{\mathrm{BH},f}}{3.0 M_\odot}\right)^{-1}[1 - 0.63(1 - a_f)^{0.3}] \text{ kHz}, \tag{4.12}$$

$$t_d \approx \frac{2(1 - a_{\mathrm{f}})^{-0.45}}{\pi f_{\mathrm{QNM}}} \text{ ms}. \tag{4.13}$$

Figures 16(a) and 16(b) show that gravitational waves for model APR1515 are well fitted by the hypothetical waveforms given by Eq. (4.11) for $t_{\mathrm{ret}} \gtrsim 10.5$ ms. [Here, we set $a_f = a_{f2}$ for the fitting (cf. Sec. IV B)]. This is reasonable because the final outcome for model APR1515 is a stationary rotating black hole with negligible disk mass, and hence, the black hole perturbation theory [i.e., Eq. (4.11)] should work well. This is also the case for the gravitational waveforms for model APR145145, for which the merger proceeds in essentially the same manner as that for model APR1515.

We note that gravitational waves emitted for $t_{\mathrm{ret}} \lesssim 10.5$ ms are not well fitted by the hypothetical fitting
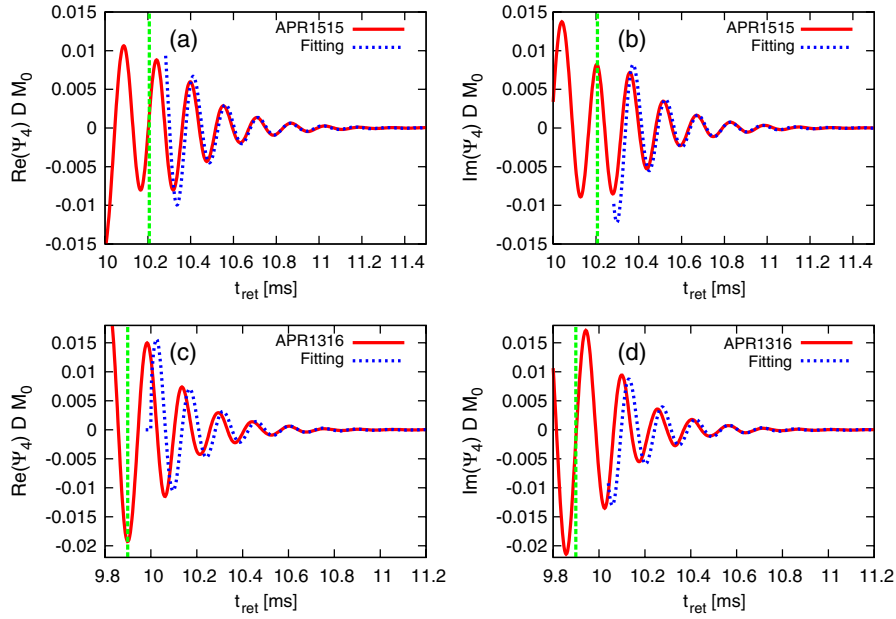

FIG. 16 (color online). Ringdown waveforms associated primarily with the fundamental quasinormal mode (a), (b) for run APR1515H and (c), (d) for run APR1316H. The panels (a) and (c) plot the real part of Ψ_4 and (b) and (d) the imaginary part. For all the panels, the short-dashed curves denote the fitting curves calculated by Eq. (4.11). The vertical dashed line in each panel denotes the formation time of the apparent horizon.
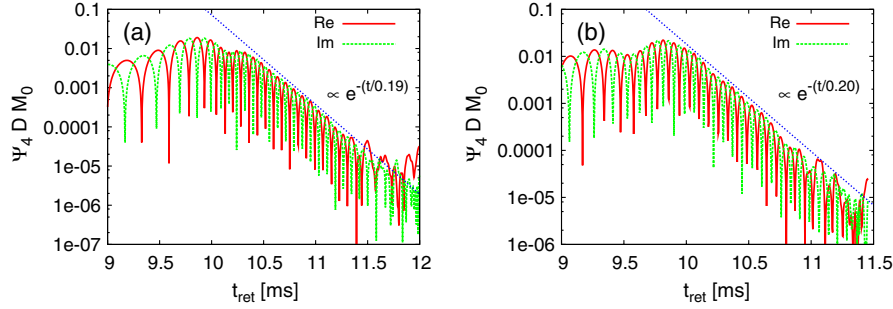
FIG. 17 (color online). Decay of Ψ_4 for (a) run APR1515H and (b) run APR1316H. Solid, dashed, and short-dashed curves denote the real, imaginary part of Ψ_4, and exponential decay with $t_d = 0.19$ ms for run APR1515H and 0.20 ms for run APR1316H.

formula. This implies that they are not the ringdown waves but merger waves. Namely, these gravitational waves are not emitted by the ringdown oscillation of the black hole but probably by a motion of the material moving around the black hole. Figures 16(a) and 16(b) show that the gravitational-wave amplitude in the merger phase is much larger than that in the ringdown phase.

The fitting between the numerical and analytic waveforms for models APR1316 and APR135165 works fairly well, but is not as good as that for models APR1515 and APR145145 [see Figs. 16(c) and 16(d) for the results of run APR1316H]; the numerical waveform may be fitted by the analytic one for $t_{\rm ret} \gtrsim 10.4$ ms, but the damping time appears to modulate. This disagreement is reasonable because for models APR1316 and APR135165, a fraction of the material is located outside the black hole horizon even after formation of the black hole, and it subsequently falls into the black hole. Thus, the system is not completely in vacuum nor in a stationary state, and hence, the numerical waveforms may not be well fitted by the analytic results derived in an ideal assumption.

Damping time scale t_d in Eq. (4.13) allows us to evaluate black hole spin. By this method, we can check the accuracy of the spin parameters estimated by the methods described in Sec IV B. Figure 17 depicts the evolution of $|\Psi_4|$ for runs APR1515 and APR1316, which shows a clear exponential decay in 10.5 ms $\lesssim t \lesssim$ 11.5 ms for APR1515 and 10 ms $\lesssim t \lesssim$ 10.5 ms for APR1316. We find that the damping time scale is estimated from this figure as 0.19 $\pm$ 0.01 ms for run APR1515H and 0.20 $\pm$ 0.02 ms for run APR1316H. The larger uncertainty for run APR1316H reflects the fact that surrounding matter falls into the black hole even after the black hole formation for a relatively long time scale and ringdown gravitational waves are not simply characterized by the fundamental quasinormal modes. Putting the values of the damping time scale into Eq. (4.13), the black hole spin is estimated as 0.77 $\pm$ 0.04 for run APR1515H and 0.84 $\pm$ 0.06 for run APR1316H. As expected, these values agree with the results in Sec. IV B within the error bar.

The merger waveforms also depend on the mass ratio. We plot the plus mode of gravitational waves (h_+) for runs

APR1515H and APR135165H in Fig. 18. To focus on waveforms just before/after BH formation, waveforms are shifted to align the formation time of the apparent horizon (vertical dashed line). The peak at $t \sim 10$ ms for model APR1515 is higher than that for model APR135165. This reflects the fact that the less massive neutron star for model APR135165 is tidally deformed from the late inspiral phase, and at the merger, the material of it starts expanding. Consequently, its compactness decreases quickly, so does the degree of nonaxisymmetry of the system, reducing the amplitude of gravitational waves.

The amplitude of the first peak after the black hole formation is, by contrast, higher for model APR135165 than for model APR1515. This seems to reflect the fact that more material is located outside the black hole horizon at the black hole formation for model APR135165, because such material subsequently falls into the black hole to excite gravitational waves.

4. Fourier spectrum

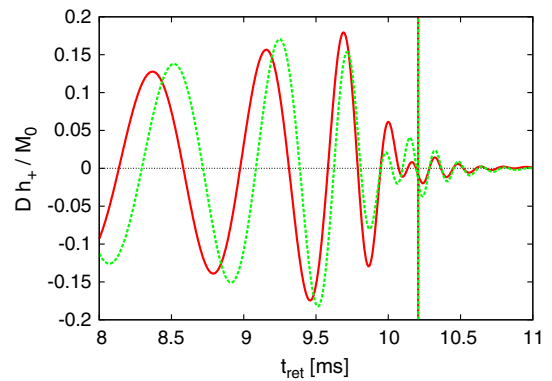We define a Fourier power spectrum of gravitational waves by

FIG. 18 (color online). The plus mode of gravitational waves (h_+) for runs APR1515H (solid curve) and APR135165H (dashed curve). The vertical dashed line denotes the formation time of apparent horizon for run APR135165H. The waveform for run APR1515H is shifted to align the formation time of the apparent horizon.

$$h(f) \equiv \sqrt{\frac{|h_+(f)|^2 + |h_\times(f)|^2}{2}}, \qquad (4.14)$$

where

$$h_+(f) = \int e^{2i\pi ft} h_+(t) dt, \qquad (4.15)$$

$$h_\times(f) = \int e^{2i\pi ft} h_\times(t) dt, \qquad (4.16)$$

and h_+ and $h_\times$ denote the $+$ and $\times$ modes of gravitational waves of $l = |m| = 2$. Then, from $h(f)$, we define a non-dimensional spectrum (or effective amplitude) as

$$h_{\text{eff}}(f) \equiv h(f)f. \qquad (4.17)$$

Figure 19 shows the spectrum (h_{eff}) of gravitational waves for runs APR1414H, APR1515H, APR1316H, and APR13516H. To plot Fig. 19, we assume $D = 100$ Mpc. Because the simulations are started with an orbit of a finite value of Ω_0 ($f \equiv \Omega_0/\pi \sim 700$ Hz), the spectrum amplitude is not realistic for a low-frequency side $f \lesssim 800$ Hz. To compensate for this drawback, we plot the spectrum of gravitational waves derived by the Taylor T4 formula by the dotted curve, which approximately behaves as $\propto f^{-n}$ where n depends weakly on f and is slightly larger than $1/6$ around $f \lesssim 1$ kHz (note that for $f \ll 1$ kHz, $n \to 1/6$ [2]). The figures show that the spectrum computed numerically smoothly connects to that of the Taylor T4 formula at ~ 0.8–1 kHz, indicating an acceptable accuracy of the numerical results.

The first noteworthy feature found from Fig. 19 is that the spectrum amplitude does not steeply damp even at $f \sim$ 1.2–1.3 kHz [82] where the binary neutron stars reach the ISCO, although this is predicted by the results derived from the Taylor T4 formula. This indicates that gravitational waves are emitted by a high-velocity motion of a merging object even after the binary neutron stars reach the ISCO. Rather, the spectrum amplitude steeply damps at a fairly high frequency $f = f_{\text{cut}} \sim$ 2.5–3 kHz for the case that a black hole is formed. This indicates that by an inspiral-type motion, gravitational waves are emitted even up to such a high frequency: Even after the onset of the merger, two high-density peaks remain in the merging object (see the fourth panel of Fig. 4), and the system emits gravitational waves for which the waveform is similar to the inspiral one.

For the case that a hypermassive neutron star is formed (for model APR1414), multiple characteristic peaks for $\sim$2–5 kHz are seen. These peaks are related to quasiperiodic gravitational waves emitted by the hypermassive neutron star. As reported in Ref. [17], the peak of the highest amplitude appears at $f \sim 3.8$ kHz for model APR1414, which is associated with gravitational waves emitted by the quasiperiodic rotation of the hypermassive neutron star. The sideband peaks are generated by the coupling modulation between the modes of the quasiperiodic rotation and of a quasiradial oscillation of the hypermassive neutron star for which the oscillation frequency is $\sim$1.2 kHz. We note that the simulation was artificially stopped at $t \sim$ 20 ms for this model, but the hypermassive neutron star is likely to survive for a longer time $\gtrsim 1$ s. Hence, the peak
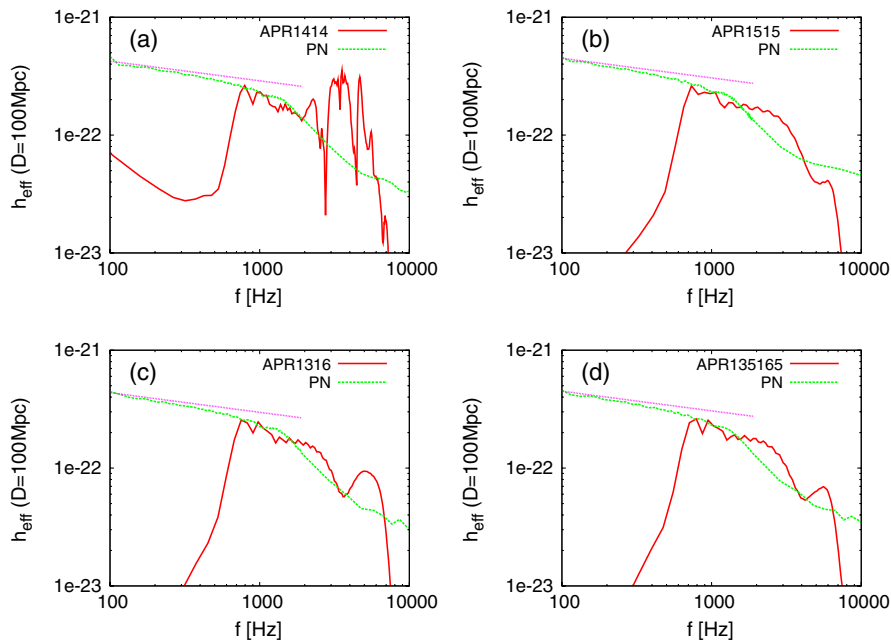

FIG. 19 (color online). Spectrum of gravitational waves as a function of frequency for runs (a) APR1414H, (b) APR1515H, (c) APR1316H, and (d) APR135165H for a hypothetical distance of 100 Mpc. For comparison, the spectrum calculated by the Taylor T4 (Newtonian quadrupole, e.g., $\propto f^{-1/6}$) formula is shown by the dashed curve (dotted line).

amplitude of the spectrum may be a factor of $\sim 7 (\sim\sqrt{1000/20})$ larger in reality. In Fig. 20(b), we plot $h(f)$ together with the planned noise level of the advanced LIGO, to clarify detectability of quasiperiodic gravitational waves emitted by the hypermassive neutron star. Based on the hypothesis that the hypermassive neutron star survives for ~ 1 s, the peak amplitudes around 3–4 kHz may be raised up by a factor of several. This suggests that such gravitational waves may be detected for an event of $D \lesssim 20$–30 Mpc, as mentioned in Refs. [17,22].

For models APR1515, APR145145, APR1316, and APR135165, the spectrum shape has qualitatively a universal feature [see Fig. 20(a)]: (i) for $f \lesssim f_{\text{cut}} \approx$ 2.5–3 kHz, the spectrum amplitude gradually decreases with f according to the relation $\propto f^{-n}$ where n takes values between 1/6 and $\sim 1/3$; (ii) for $f \gtrsim f_{\text{cut}}$, the amplitude steeply decreases. This is likely to reflect the fact that two high-density peaks in the merged object disappear during the collapse to a black hole; (iii) for $f = f_{\text{peak}} \approx 5$–6 kHz, which is slightly smaller than $f_{\text{QNM}} \approx 6.5$–6.9 kHz, a broad peak appears. Because the frequency is always smaller than f_{QNM}, this peak is not associated with the ringdown gravitational waveform but with the merger waveform; it is likely to be emitted by matter moving around the black hole; (iv) for $f > f_{\text{fin}} \approx f_{\text{QNM}}$, the amplitude damps in an exponential manner.

We note that the feature of the spectrum shape is qualitatively similar to that for the merger of binary black holes [47], except for the following differences: One of the most noticeable differences is found in phase (ii). For the case of binary neutron stars, the spectrum amplitude steeply decreases for $f \gtrsim f_{\text{cut}}$. By contrast for binary black holes such a steep decrease is not found. The other remarkable difference is found in the peak amplitude associated with phase (iii) and (iv): For the binary neutron stars, this is at almost half of the amplitude at the ISCO ($f \sim 1$ kHz for the binary neutron stars), whereas for binary black holes, this peak amplitude is as large as or even larger than the amplitude at the ISCO (e.g., Ref. [47]).

The spectrum shape in the case of black hole formation is significantly different from that of hypermassive neutron star formation for $f \gtrsim 2$ kHz. Figure 20(b) compares the spectra for models APR1414 and APR145145. For model APR1414, there are multiple spiky peaks in the spectrum for 2 kHz $\lesssim f \lesssim 6$ kHz. By contrast, the spectrum shape is fairly smooth for model APR145145. This suggests that if gravitational waves of frequency between about 2 kHz and 6 kHz are detected, the outcome (hypermassive neutron star or black hole) can be distinguished.

The most remarkable difference among the spectrum shapes of the four black-hole formation models shown in Fig. 20(a) is found in the amplitude and width of the peak associated with the merger waveform: The peak amplitude for models APR1515 and APR145145 is much less prominent than that for models APR135165 and APR1316 [see Fig. 20(a) and compare the same-mass models], reflecting the fact that the amplitude of the merger gravitational waveform is smaller. This difference seems to reflect the difference in the disk-formation process, as mentioned in
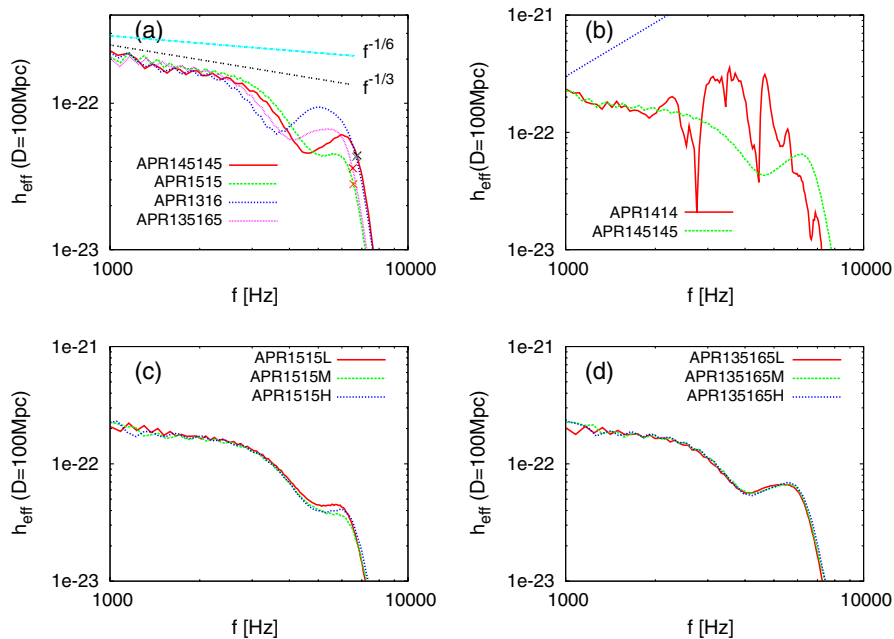

FIG. 20 (color online). (a) Spectrum of gravitational waves for runs APR145145H, APR1515H, APR1316H, and APR135165H, (b) spectrum for runs APR1414H and APR145145H, (c) the spectrum for runs APR1515L, APR1515M, and APR1515H, and (d) the spectrum for runs APR135165L, APR135165M, and APR135165H. Lines and cross symbols in the panel (a) denote $f^{-1/6}$, $f^{-1/3}$, and QNM frequencies for all the models. The dotted line in the panel (b) shows the planned noise level of the advanced LIGO.

Sec. IV C 3: For the equal-mass models, nearly all the material simultaneously collapse to a black hole, whereas for the unequal-mass models, disks surrounding the black hole are formed and subsequently the material of the disk fall into the black hole, enhancing the amplitude of gravitational waves. This difference in the accretion process is also reflected in the width of the peak: For the unequal-mass models, the width of the peak is broader. This indicates that a variety of the matter motion induces those gravitational waves.

The merger process is also reflected in the value of f_{cut}. For equal-mass runs APR145145H and APR1515H, $f_{cut} \sim$ 3.0 kHz, while for unequal-mass runs APR1316H and APR135165H, $f_{cut} \sim 2.5$ kHz (f_{cut} does not depend strongly on the grid resolution). Thus, f_{cut} is smaller for the unequal-mass models for a given value of the total mass. The reason for this is that tidal elongation and disruption of the less massive neutron star occur for the unequal-mass binary neutron stars in the late inspiral phase. The tidal elongation sets in at a relatively low frequency just after the binary neutron stars reach the ISCO. This is reflected in a steep decrease of the spectrum amplitude at a smaller frequency.

The total mass of the system is reflected in the value of f_{fin}. Figure 20(a) shows that the frequency at which h_{eff} reaches 2×10^{-23} (for $D = 100$ Mpc) is approximately inversely proportional to the total mass; e.g., $f_{fin} \sim$ 7.2 kHz for models APR1515 and APR135165 and $f_{fin} \sim$ 7.6 kHz for models APR145145 and APR1316. This is reasonable because the value of f_{fin} is determined primarily by f_{QNM} which is inversely proportional to the black hole mass for a given spin, and hence, approximately to the total mass.

Before closing this section, we comment on the convergence. Figures 20(c) and 20(d) plots the spectrum for runs APR1515L, APR1515M, and APR1515H and that for runs APR135165L, APR135165M, and APR135165H, respectively. This shows that these do not overlap completely, but the amplitude for a given frequency agrees among three results within $\sim 1 \times 10^{-23}$ error for both models. Such error does not affect the findings and conclusions in this section.

V. SUMMARY

This paper reports new numerical results of general relativistic simulations for binary neutron stars, focusing, in particular, on the case that a black hole is formed in dynamical time scale after the onset of merger. Following Ref. [17], the APR EOS and irrotational velocity field are employed for modeling the binary neutron stars in the inspiral phase. We prepare initial conditions with an orbital separation which is much larger than that in the previous work [17], and hence, unphysical effects associated with initial nonzero eccentricity and incorrect approaching velocity are excluded with a much better manner. We adopt

the moving-puncture approach, which enables to simulate black hole formation and subsequent long-term evolution of the black hole spacetime. Furthermore, the simulations are performed with a much better grid resolution than that in the previous work [17] to obtain more reliable numerical results.

As a result of the improvements summarized above, we have obtained the following new results for the outcome formed after the merger in the present work: (i) For the binary neutron stars modeled by the APR EOS, a black hole is formed in the dynamical time scale after the onset of the merger, if the total mass of the system m_0 is larger than a threshold mass $M_{thr} = 2.8$–$2.9M_\odot$. This holds irrespective of the mass ratio as long as $0.8 \lesssim Q_M \leq 1$. In the present work, the value of M_{thr} is determined with less uncertainty than that in Ref. [17]. (ii) For the case that the black hole is formed in the dynamical time scale after the onset of the merger, the resulting black hole spin a_f is $\approx 0.78 \pm 0.02$. This value depends weakly on the total mass and mass ratio of the binary neutron stars. (iii) The mass of the formed black hole, $M_{BH,f}$, is calculated from the approximate energy conservation relation (4.3) and the circumferential equatorial radius of apparent horizon within $\approx 0.5\%$ error. (iv) The mass and spin of the formed black hole are consistent with those determined by the frequency and damping time of the quasinormal mode of gravitational waves, even when a disk of mass $\lesssim 0.03M_\odot$ is formed around the black hole. (v) A quasisteady disk of mass $\gtrsim 0.01M_\odot$ is formed around the black hole for the mass ratio $Q_M \approx 0.8$. The disk mass depends not only on the mass ratio but also on the total mass of the binary neutron stars. We find that for the total mass (m_0) closer to M_{thr}, the resulting disk mass is larger.

Gravitational waves emitted during the merger and ringdown phases are also analyzed. For the case that a hypermassive neutron star is formed, gravitational waves are composed of the inspiral, merger, and quasiperiodic waveforms. The quasiperiodic waves are emitted due to quasiperiodic rotation of the formed ellipsoidal hypermassive neutron star. For model APR1414, its characteristic frequency is ≈ 3.8 kHz, which agrees with that found in the previous paper [17]. As mentioned in the previous works [17,22], the effective amplitude for the quasiperiodic waves could be larger than $\sim 10^{-21}$ at a distance of $D \leq$ 100 Mpc. Although the frequency is rather high and slightly outside the best-sensitive band of ground-based gravitational-wave detectors, such gravitational waves are an interesting target for the next-generation interferometric detectors.

For the case that a black hole is formed in the dynamical time scale after the onset of the merger, gravitational waves are composed of the inspiral, merger, and ringdown waveforms. The feature is qualitatively universal, irrespective of the total mass and mass ratio of the binary neutron stars. The feature is clearly seen in the Fourier spectrum, and

quantitatively summarized as follows: (i) For $f \lesssim f_{cut} \approx$ 2.5–3 kHz, the spectrum amplitude gradually decreases according to the relation $\propto f^{-n}$ where n is a slowly varying function of f; $n = 1/6$ for $f \ll 1$ kHz, and $n \sim 1/3$ for $f \to f_{cut}$. f_{cut} is much larger than the frequency at the ISCO. This is due to the fact that even after the onset of the merger, the merging object has two high-density peaks, and emits gravitational waves for which the waveform is similar to the inspiral one. (ii) For $f \gtrsim f_{cut}$, the spectrum amplitude steeply decreases. This seems to reflect the fact that at such frequency, two density peaks disappear during the collapse to a black-hole. (iii) For $f = f_{peak} \approx$ 5–6 kHz, which is slightly smaller than $f_{QNM} \sim$ 6.5–6.9 kHz, a broad peak appears. Because the frequency is always smaller than f_{QNM}, this peak is not associated with the ringdown gravitational waveform but with the merger waveform. (iv) For $f > f_{fin} \approx f_{QNM}$, the amplitude damps in an exponential manner.

Although the features (i)–(iv) are qualitatively universal, the values of f_{cut}, f_{peak}, f_{QNM}, and f_{fin}, and the height and width of the peak at $f = f_{peak}$ depend on the total mass and mass ratio of binary neutron stars, i.e., merger and black hole formation processes. This implies that if gravitational waves of high frequency $f = 2$–8 kHz are detected, we will be able to get information about merger and black hole formation precesses.

As mentioned in Sec. I, the hybrid EOS adopted in this work seems to be appropriate for studying black hole formation in the merger of the binary neutron stars. However, for studying hypermassive neutron star formation or evolution of accretion disk around the formed black hole, the present choice of the EOS is not very appropriate, because for such cases, effects associated with the thermal energy (finite temperature) and neutrino cooling are likely to play an important role (e.g., Ref. [83]). Magnetic fields will also play an important role for long-term evolution of

the hypermassive neutron star and black hole-accretion disks if they are amplified in a short time scale (say in 10 dynamical time scales of the system). In a future paper, we would like to report our new studies in which these effects are taken into account.

In the present work, we are not able to compute the inspiral waveforms with a high precision because the grid resolution is not high enough. Even with the highest-grid resolution (e.g., in run APR1515H), the phase error may amount to 2 wave cycles (see Fig. 13). To suppress the phase error within, e.g., a half wave cycle in the inspiral phase, the grid resolution would have to be 30%–40% as high as that for model APR1515H. To perform such high-resolution simulation, the present choice of the grid structure requires a high computational cost, in particular, for a systematic survey of gravitational waveforms for a variety of parameters. We have to adopt an AMR algorithm [25,26,79] to save the computational cost. Currently, we are studying the inspiral waveforms in the simulation using a code with the AMR algorithm [25]. We hope to present such results in the near future.

ACKNOWLEDGMENTS

[1] B. C. Barish and R. Weiss, Phys. Today **52**, No. 10, 44 (1999).

[2] C. Cutler and K. S. Thorne, in *Proceedings of the 16th International Conference on General Relativity and Gravitation*, edited by N. T. Bishop and S. D. Mharaj (World Scientific, Singapore, 2002), p. 72.

[3] S. Hild, Classical Quantum Gravity **23**, S643 (2006).

[4] F. Acernese *et al.* (VIRGO Collaboration), Classical Quantum Gravity **19**, 1421 (2002).

[5] F. Acernese *et al.*, Classical Quantum Gravity **23**, S635 (2006).

[6] K. Tsubono, in Edoardo Amaldi Meeting on Gravitational Wave Experiments, Rome, Italy, 1994.

[7] V. Kalogera *et al.*, Astrophys. J. **601**, L179 (2004); **614**, L137(E) (2004).

[8] K. Belczynski *et al.*, Astrophys. J. **662**, 504 (2007): This paper suggests that the merger rate may be much lower than that predicted by the earlier works [7].

[9] R. Narayan, B. Paczynski, and T. Piran, Astrophys. J. **395**, L83 (1992).

[10] B. Zhang and P. Meszaros, Int. J. Mod. Phys. A **19**, 2385 (2004).

[11] D. B. Fox *et al.*, Nature (London) **437**, 845 (2005).

[12] T. Piran, Rev. Mod. Phys. **76**, 1143 (2005).

[13] R. Popham, S. E. Woosley, and C. Fryer, Astrophys. J. **518**, 356 (1999); T. Di Matteo, R. Perna, and R. Narayan, Astrophys. J. **579**, 706 (2002); A. Janiuk, A. R. Perna, T. Di Matteo, and B. Czerny, Mon. Not. R. Astron. Soc. **355**, 950 (2004).

[14] S. Setiawan, M. Ruffert, and H.-Th. Janka, Mon. Not. R.

Astron. Soc. **352**, 753 (2004); Astron. Astrophys. **458**, 553 (2006); W. H. Lee, E. Ramirez-Ruiz, and D. Page, Astrophys. J. **632**, 421 (2005); M. Shibata, Y. I. Sekiguchi, and R. Takahashi, Prog. Theor. Phys. **118**, 257 (2007).

[15] J. C. McKinney and C. F. Gammie, Astrophys. J. **611**, 977 (2004); J. C. McKinney, Mon. Not. R. Astron. Soc. **368**, 1561 (2006); J. F. Hawley and J. H. Krolik, Astrophys. J. **641**, 103 (2006).

[16] R. D. Blandford and R. L. Znajek, Mon. Not. R. Astron. Soc. **179**, 433B (1977).

[17] M. Shibata and K. Taniguchi, Phys. Rev. D **73**, 064027 (2006).

[18] M. Shibata, Phys. Rev. D **60**, 104052 (1999).

[19] M. Shibata and K. Uryu, Phys. Rev. D **61**, 064001 (2000).

[20] M. Shibata and K. Uryu, Prog. Theor. Phys. **107**, 265 (2002).

[21] M. Shibata, K. Taniguchi, and K. Uryu, Phys. Rev. D **68**, 084020 (2003).

[22] M. Shibata, K. Taniguchi, and K. Uryu, Phys. Rev. D **71**, 084021 (2005); M. Shibata, Phys. Rev. Lett. **94**, 201101 (2005).

[23] M. A. Miller, P. Gressman, and W. M. Suen, Phys. Rev. D **69**, 064026 (2004).

[24] P. Marronetti, M. D. Duez, S. L. Shapiro, and T. W. Baumgarte, Phys. Rev. Lett. **92**, 141101 (2004).

[25] T. Yamamoto, M. Shibata, and K. Taniguchi, Phys. Rev. D **78**, 064054 (2008).

[26] L. Baiotti, B. Giacomazzo, and L. Rezzolla, Phys. Rev. D **78**, 084033 (2008)

[27] In the simulation for nonspinning equal-mass binary black holes, effects of orbital eccentricity, and initial orbital separation on the merger dynamics discussed in Refs. [28,29], they suggest that if the orbital eccentricity is less than 0.5, mass and spin of the formed black hole depend weakly on the eccentricity. A similar statement holds for the initial orbital separation, if the orbit is quasicircular. However, whether this result holds for binary neutron star merger or not is unclear because in contrast to the merger of binary black holes, hydrodynamic processes play an essential role in the merger of binary neutron stars.

[28] I. Hinder et al., Phys. Rev. D **77**, 081502 (2008).

[29] U. Sperhake et al., Phys. Rev. D **78**, 064069 (2008).

[30] M. Campanelli, C. O. Lousto, P. Marronetti, and Y. Zlochower, Phys. Rev. Lett. **96**, 111101 (2006); J. G. Baker et al., Phys. Rev. Lett. **96**, 111102 (2006).

[31] B. Brugmann et al., Phys. Rev. D **77**, 024027 (2008).

[32] M. Boyle et al., Phys. Rev. D **76**, 124038 (2007);

[33] M. Shibata and K. Uryu, Phys. Rev. D **74**, 121503 (2006); Classical Quantum Gravity **24**, S125 (2007).

[34] M. Shibata and K. Taniguchi, Phys. Rev. D **77**, 084015 (2008).

[35] Y. T. Liu, S. L. Shapiro, Z. B. Etienne, and K. Taniguchi, Phys. Rev. D **78**, 024012 (2008).

[36] A. Akmal, V. R. Pandharipande, and D. G. Ravenhall, Phys. Rev. C **58**, 1804 (1998).

[37] H. Shen, H. Toki, K. Oyamatsu, and K. Sumiyoshi, Nucl. Phys. **A637**, 435 (1998); Prog. Theor. Phys. **100**, 1013 (1998).

[38] J. M. Lattimer and M. Prakash, Astrophys. J. **550**, 426

(2001).

[39] J. M. Lattimer and F. D. Swesty, Nucl. Phys. **A535**, 331 (1991).

[40] M. Shibata and T. Nakamura, Phys. Rev. D **52**, 5428 (1995); see also, T. W. Baumgarte and S. L. Shapiro, Phys. Rev. D **59**, 024007 (1998).

[41] M. Shibata, Astrophys. J. **595**, 992 (2003).

[42] M. Shibata, Phys. Rev. D **55**, 2002 (1997).

[43] M. Shibata and K. Uryu, Phys. Rev. D **62**, 087501 (2000).

[44] A. Kurganov and E. Tadmor, J. Comput. Phys. **160**, 241 (2000).

[45] M. Shibata, Phys. Rev. D **67**, 024033 (2003).

[46] P. Haensel and A. Y. Potekhin, Astron. Astrophys. **428**, 191 (2004).

[47] A. Buonanno, G. B. Cook, and F. Pretorius, Phys. Rev. D **75**, 124018 (2007).

[48] M. Hannam et al., Phys. Rev. D **77**, 044020 (2008).

[49] M. A. Scheel et al., Phys. Rev. D **79**, 024003 (2009).

[50] M. Boyle and A. H. Mroue, arXiv:0905.3177.

[51] M. Hannam, Classical Quantum Gravity **26**, 114001 (2009).

[52] L. Blanchet, Living Rev. Relativity **9**, 4 (2006).

[53] P. Ajith et al., Phys. Rev. D **77**, 104017 (2008).

[54] M. Hannam, S. Husa, B. Bruegmann, and A. Gopakumar, Phys. Rev. D **78**, 104007 (2008).

[55] M. Boyle et al., Phys. Rev. D **78**, 104020 (2008).

[56] J. G. Baker et al., Phys. Rev. Lett. **99**, 181101 (2007).

[57] S. L. Shapiro and S. A. Teukolsky, *Black Holes, White Dwarfs, and Neutron Stars* (Wiley-Interscience, New York, 1983), p. 645.

[58] G. B. Cook, Living Rev. Relativity **3**, 5 (2000).

[59] C. S. Kochanek, Astrophys. J. **398**, 234 (1992).

[60] L. Bildsten and C. Cutler, Astrophys. J. **400**, 175 (1992).

[61] E. Gourgoulhon et al., Phys. Rev. D **63**, 064029 (2001).

[62] K. Taniguchi and E. Gourgoulhon, Phys. Rev. D **66**, 104019 (2002).

[63] K. Taniguchi and E. Gourgoulhon, Phys. Rev. D **68**, 124025 (2003).

[64] LORENE website: http://www.lorene.obspm.fr/.

[65] P. C. Peters and J. Mathews, Phys. Rev. **131**, 435 (1963).

[66] H. P. Pfeiffer et al., Classical Quantum Gravity **24**, S59 (2007).

[67] S. Husa et al., Phys. Rev. D **77**, 044037 (2008).

[68] B. Bruegmann et al., Phys. Rev. D **77**, 124047 (2008).

[69] T. W. Baumgarte, S. L. Shapiro, and M. Shibata, Astrophys. J. Lett. **528**, L29 (2000).

[70] S. Chandrasekhar, *Ellipsoidal Figures of Equilibrium* (Yale University Press, New Haven, 1969); J.-L. Tassoul, *Theory of Rotating Stars* (Princeton University Press, Princeton, 1978).

[71] S. A. Balbus and J. F. Hawley, Astrophys. J. **376**, 214 (1991).

[72] M. Shibata, Y. T. Liu, S. L. Shapiro, and B. C. Stephens, Phys. Rev. D **74**, 104026 (2006).

[73] M. D. Duez, Y. T. Liu, S. L. Shapiro, and M. Shibata, Phys. Rev. D **73**, 104015 (2006).

[74] M. Shibata, K. Kyotoku, T. Yamamoto, and K. Taniguchi, Phys. Rev. D **79**, 044030 (2009).

[75] M. Shibata, Phys. Rev. D **76**, 064035 (2007).

[76] D. Lai, F. A. Rasio, and S. L. Shapiro, Astrophys. J. Suppl. Ser. **88**, 205 (1993).

[77] A. Gopakumar, M. Hannam, S. Husa, and B. Bruegmann, Phys. Rev. D **78**, 064026 (2008).

[78] M. Boyle, D. A. Brown, and L. Pekowsky, Classical Quantum Gravity **26**, 114006 (2009).

[79] M. Anderson *et al.*, Phys. Rev. D **77**, 024006 (2008).

[80] E. W. Leaver, Proc. R. Soc. A **402**, 285 (1985).

[81] F. Echeverria, Phys. Rev. D **40**, 3194 (1989).

[82] M. Bejger *et al.*, Astron. Astrophys. **431**, 297 (2005).

[83] M. Ruffert, H. T. Ruffert, and H. T. Janka, Astron. Astrophys. **380**, 544 (2001).